Applied Numerical Mathematics 93 (2015) 215–241

Contents lists available at ScienceDirect

Applied Numerical Mathematics

www.elsevier.com/locate/apnum

Computation of singular solutions to the Helmholtz equation with high order accuracy ☆

S. Britt [a], S. Petropavlovsky [a,b], S. Tsynkov [a,c,*], E. Turkel [d]

[a] Department of Mathematics, North Carolina State University, Box 8205, Raleigh, NC 27695, USA
[b] Department of Applied Mathematics, Financial University under the Government of the Russian Federation, Moscow 125993, Russia
[c] Moscow Institute of Physics and Technology, Dolgoprudny, 141700, Russia
[d] School of Mathematical Sciences, Tel Aviv University, Ramat Aviv, Tel Aviv 69978, Israel

ARTICLE INFO

Article history:
Available online 13 November 2014

This paper is dedicated to Prof. Victor S. Ryaben'kii on the occasion of his 90th Birthday

Keywords:
Difference potentials
Boundary projections
Calderon's operators
Regular grids
Curvilinear boundaries
Non-conforming boundaries
Solutions with singularities
Singularity subtraction
Discontinuous boundary data
Asymptotic expansion near singularity
Compact differencing
High order accuracy

ABSTRACT

Solutions to elliptic PDEs, in particular to the Helmholtz equation, become singular near the boundary if the boundary data do not possess sufficient regularity. In that case, the convergence of standard numerical approximations may slow down or cease altogether. We propose a method that maintains a high order of grid convergence even in the presence of singularities. This is accomplished by an asymptotic expansion that removes the singularities up to several leading orders, and the remaining regularized part of the solution can then be computed on the grid with the expected accuracy.

The computation on the grid is rendered by a compact finite difference scheme combined with the method of difference potentials. The scheme enables fourth order accuracy on a narrow 3×3 stencil: it uses only one unknown variable per grid node and requires only as many boundary conditions as needed for the underlying differential equation itself. The method of difference potentials enables treatment of non-conforming boundaries on regular structured grids with no deterioration of accuracy, while the computational complexity remains comparable to that of a conventional finite difference scheme on the same grid. The method of difference potentials can be considered a generalization of the method of Calderon's operators in PDE theory.

In the paper, we provide a theoretical analysis of our combined methodology and demonstrate its numerical performance on a series of tests that involve Dirichlet and Neumann boundary data with various degrees of "non-regularity": an actual jump discontinuity, a discontinuity in the first derivative, a discontinuity in the second derivative, etc. All computations are performed on a Cartesian grid, whereas the boundary of the domain is a circle, chosen as a simple but non-conforming shape. In all cases, the proposed methodology restores the design rate of grid convergence, which is fourth order, in spite of the singularities and regardless of the fact that the boundary is not aligned with the discretization grid. Moreover, as long as the location of the singularities is known and remains fixed, a broad spectrum of problems involving different boundary conditions and/or data on "smooth" segments of the boundary can be solved economically since the

☆ Work supported by the US–Israel Binational Science Foundation (BSF) under Grant # 2008094, by the US ARO under Grant # W911NF-11-1-0384, and by the US AFOSR under Grant # FA9550-10-1-0092.

* Corresponding author at: Department of Mathematics, North Carolina State University, Box 8205, Raleigh, NC 27695, USA.
E-mail addresses: dsbritt@ncsu.edu (S. Britt), SPetropavlovsky@fa.ru (S. Petropavlovsky), tsynkov@math.ncsu.edu (S. Tsynkov), turkel@post.tau.ac.il (E. Turkel).
URLs: http://www.math.ncsu.edu/~stsynkov (S. Tsynkov), http://www.math.tau.ac.il/~turkel/ (E. Turkel).

http://dx.doi.org/10.1016/j.apnum.2014.10.006

discrete counterparts of Calderon's projections need to be calculated only once and then can be applied to each individual formulation at very little additional cost.

1. Introduction

In our previous work [4], we have shown how a numerical methodology that combines compact fourth order accurate schemes [8,17,3] with the method of difference potentials [15,13,14] applies to solving a variety of non-standard boundary value problems for the Helmholtz equation. The formulations investigated in [4] involved variable coefficient Robin, as well as discontinuous and mixed Dirichlet and Neumann boundary conditions. In all cases, the method of difference potentials has enabled an efficient and accurate account of a given boundary condition when the curvilinear boundary was not aligned with the discretization grid, whereas the compact scheme has provided an easy and inexpensive venue toward high order accuracy, which is critical in wave applications [2,9,6,1]. However, when the solution did not possess sufficient regularity, the convergence rate of the overall method was considerably slower than the fourth order design rate. In general, the solution may have lower regularity due to a discontinuity in the coefficients of the boundary condition and/or the boundary data. In that case, a near-boundary singularity develops and the finite difference scheme loses consistency, which translates into a (much) slower convergence rate.

In the current paper, we show how the design convergence rate for the combined methodology of [4] can be restored in the case where the solution may have such near-boundary singularities. The idea is to subtract out several leading terms in the expansion of the solution near the singular point, and subsequently solve only for the remaining regular component. In developing the expansion, we follow the approach earlier proposed in [7] and modify it so as to take into account that the segments of the boundary meeting at a given singular point may be curves rather than only straight lines. We also note that an earlier work that addresses singularities of the solution using difference potentials is presented in [11,10,12]; however, it does not involve computations with high order accuracy.

The paper is organized as follows. In Section 1.1, we introduce the formulation of the problem that we subsequently study. In Sections 1.2, 1.3, and 1.4, we provide brief accounts of the compact scheme and the method of difference potentials, while referring the reader for detail to earlier, more comprehensive publications. In Section 1.5, we show how to take into account various boundary conditions specified on different segments of the boundary.

Then, in Section 2 we analyze the near-boundary singularities which result from discontinuities in the boundary data. In doing so, we describe in Section 2.1 how the general approach of [7] applies to our specific formulations of interest (introduced in Section 1.1), in Section 2.2 we discuss how it can be generalized for the case of boundaries with curvature, and in Section 2.3 we choose and solve specific examples (the account of these examples is continued in Appendix A). In Section 3, we apply the method of difference potentials to a problem with near-boundary singularities. In particular, in Section 3.1 we show how to modify the problem by subtracting singular terms so that the regularity of the remaining solution increases, and in Section 3.2 we demonstrate how the entire family of problems that have the same singular points but may otherwise be different can be solved at a low cost per problem. In Section 4, we corroborate the previously developed theory by a series of computations for discontinuous boundary conditions of both Dirichlet and Neumann type that lead to singularities of various strength depending on the varying degree of discontinuity in the data. Finally, in Section 5 we present our conclusions and discuss the future work.

1.1. Formulation of the problem

Consider a bounded domain $\Omega \subset \mathbb{R}^2$ and denote its boundary by Γ: $\Gamma = \partial\Omega$. We will be solving the homogeneous Helmholtz equation with a fixed wavenumber k on this domain:

$$\boldsymbol{L}u \stackrel{\text{def}}{=} \Delta u + k^2 u = 0, \quad \boldsymbol{x} \in \Omega, \tag{1a}$$

subject to the boundary condition

$$\boldsymbol{l}_\Gamma u = \phi_\Gamma, \quad \boldsymbol{x} \in \Gamma. \tag{1b}$$

For the purposes of this paper, the boundary condition (1b) will be either Dirichlet ($\boldsymbol{l}_\Gamma = 1$) or Neumann ($\boldsymbol{l}_\Gamma = \frac{\partial}{\partial \boldsymbol{n}}$), although the methods presented hereafter extend to the case where (1b) is of a mixed type (Dirichlet/Neumann). The boundary data in (1b) will be intentionally chosen to be discontinuous. Namely, the function $\phi_\Gamma = \phi_\Gamma(s)$, where s is the arc length, will have either jump discontinuities of its own or jump discontinuities in its first or second derivative with respect to s.

The aforementioned discontinuities in ϕ_Γ or its derivatives will cause the solution u to possess singularities at the corresponding boundary points. The analysis of Section 2 allows us to remove those near-boundary singularities (to several leading orders), and yields a new regularized boundary value problem (BVP) for the inhomogeneous Helmholtz equation, which we then solve numerically:

$$\boldsymbol{L}u = f, \quad \boldsymbol{x} \in \Omega, \tag{2a}$$

$$\boldsymbol{l}_\Gamma u = \psi_\Gamma, \quad \boldsymbol{x} \in \Gamma. \tag{2b}$$

For simplicity, we consider only the case where the domain Ω is a disk of radius $R = 1$ centered at the origin, so that its boundary Γ is a circle. From the standpoint of treating singularities that result from discontinuous boundary data, this choice presents no loss of generality. To solve the BVP (2a–2b) we introduce a Cartesian grid and implement a high order accurate finite difference scheme along with the method of difference potentials.

1.2. Compact schemes

We use a high order scheme in order to reduce the phase error due to the pollution effect [2,9,6,1]. Compact differencing offers a convenient and efficient way of building such schemes without having to impose additional, purely numerical, boundary conditions. We implement the fourth-order accurate approximation for the Helmholtz equation (2a) first introduced in [8,17]:

$$\begin{aligned}
&\frac{1}{h^2}(u_{m+1,n} + u_{m,n+1} + u_{m-1,n} + u_{m,n-1} - 4u_{m,n}) + \frac{1}{6h^2}\big[u_{m+1,n+1} + u_{m+1,n-1} + u_{m-1,n+1} - u_{m-1,n-1} + 4u_{m,n} \\
&\quad - 2(u_{m,n+1} + u_{m,n-1} + u_{m+1,n} + u_{m-1,n})\big] + \frac{k^2}{12}(u_{m+1,n} + u_{m,n+1} + 8u_{m,n} + u_{m-1,n} + u_{m,n-1}) \\
&\quad = f_{m,n} + \frac{1}{12}(f_{m+1,n} + f_{m,n+1} - 4f_{m,n} + f_{m-1,n} + f_{m,n-1}) \stackrel{\text{def}}{=} \tilde{f}_{m,n}.
\end{aligned} \tag{3}$$

Scheme (3) is built on a square-cell Cartesian grid with step size h. The left-hand side operates on u via a 9-node (3×3) compact stencil. The right-hand side $\tilde{f}$ consists of a 5-node stencil operating on f, which is the right-hand side of the inhomogeneous Helmholtz equation (2a).

We restrict the present discussion to the constant coefficient Laplacian and constant wavenumber k, although similar high order schemes can be built for variable coefficients as well. For example, in [3] a compact fourth-order accurate scheme is derived for a more general form of the Helmholtz equation with a variable-coefficient analogue of the Laplacian and a variable wavenumber k. Moreover, in [18] a sixth order compact scheme is built for the Helmholtz equation with variable k.

1.3. Auxiliary problem

The method of difference potentials requires that we enclose the domain Ω within an auxiliary domain Ω_0: $\Omega \subset \Omega_0$. On the domain Ω_0, we pose a special auxiliary problem (AP) for the inhomogeneous Helmholtz equation, $\boldsymbol{L}u = g$. The key requirement of the AP is that it has to have a unique solution for any right-hand side g defined on Ω_0. It can otherwise be formulated arbitrarily, and it is natural to choose it so that it admits a simple numerical solution. In the method of difference potentials, the AP is used for computing the discrete counterparts of Calderon's operators [5,16], and while the operators themselves will depend on the choice of the AP, see Section 1.4, the actual solution of the problem of interest, i.e., the BVP (2a–2b), will not be affected [15].

For our specific setting, we take Ω_0 as a square of side length 2.2 centered at the origin, and formulate the following AP:

$$\begin{aligned}
&\boldsymbol{L}u = g, \quad \boldsymbol{x} \in \Omega_0, \\
&u = 0, \quad y = \pm 1.1, \\
&\frac{\partial u}{\partial x} + iku = 0, \quad x = 1.1, \\
&\frac{\partial u}{\partial x} - iku = 0, \quad x = -1.1.
\end{aligned} \tag{4}$$

The AP (4) can be efficiently solved by separation of variables, and the Sommerfeld-type boundary conditions imposed on the left and right edges of the auxiliary domain (the square Ω_0) make its spectrum essentially complex and hence ensure uniqueness of the solution.

Applying the compact scheme (3) to the differential equation $\boldsymbol{L}u = g$ of (4), we have:

$$\begin{aligned}
&\frac{1}{h^2}(u_{m+1,n} + u_{m,n+1} + u_{m-1,n} + u_{m,n-1} - 4u_{m,n}) + \frac{1}{6h^2}\big[u_{m+1,n+1} + u_{m+1,n-1} + u_{m-1,n+1} - u_{m-1,n-1} + 4u_{m,n} \\
&\quad - 2(u_{m,n+1} + u_{m,n-1} + u_{m+1,n} + u_{m-1,n})\big] + \frac{k^2}{12}(u_{m+1,n} + u_{m,n+1} + 8u_{m,n} + u_{m-1,n} + u_{m,n-1}) = \tilde{g}_{m,n}.
\end{aligned} \tag{5a}$$

In doing so, we emphasize that when actually computing the difference potentials and projections (Section 1.4) the discrete right-hand side $\tilde{g}_{m,n}$ of Eq. (5a) is specified directly rather than by applying the 5-node stencil to g, so that the explicit form of g is never needed and thus never introduced.

In order to maintain the overall accuracy of the solution, it is necessary to approximate the boundary conditions of (4) with accuracy matching that of the finite difference scheme, which is fourth order in our case. The approximation is easily obtained for the Dirichlet conditions:

$$u_{m,0} = u_{m,M} = 0, \quad m = 0, \ldots, M, \tag{5b}$$

where the grid nodes range between 0 and M in both the x and y directions since we are using square cells on a square domain.

For the Sommerfeld-type conditions on the left and right edges of the square Ω_0, we implement a simplified version of the fourth-order accurate approximation derived in [3] for the Helmholtz equation with variable coefficients:

$$\begin{aligned}&\left(\frac{u_{M,n}-u_{M-1,n}}{h} - \frac{1}{6h}(u_{M,n+1}-u_{M-1,n+1}+u_{M,n-1}-u_{M-1,n-1}-2(u_{M,n}-u_{M-1,n}) - \frac{k^2h}{24}(u_{M,n}-u_{M-1,n})\right)\\&\quad + ik\left(\frac{u_{M,n}+u_{M-1,n}}{2} + \frac{h^2k^2}{8}u_{M-\frac{1}{2},n} + \frac{u_{M-\frac{1}{2},n+1} - 2u_{M-\frac{1}{2},n-1} + u_{M-\frac{1}{2},n-1}}{2}\right) = 0,\end{aligned} \tag{5c}$$

$$\begin{aligned}&\left(\frac{u_{1,n}-u_{0,n}}{h} - \frac{1}{6h}(u_{1,n+1}-u_{0,n+1}+u_{1,n-1}-u_{0,n-1}-2(u_{1,n}-u_{0,n})) - \frac{k^2h}{24}(u_{1,n}-u_{0,n})\right)\\&\quad - ik\left(\frac{u_{1,n}+u_{0,n}}{2} + \frac{h^2k^2}{8}u_{\frac{1}{2},n} + \frac{u_{\frac{1}{2},n+1} - 2u_{\frac{1}{2},n-1} + u_{\frac{1}{2},n-1}}{2}\right) = 0.\end{aligned} \tag{5d}$$

In formulae (5c) and (5d), the Sommerfeld-type conditions are enforced at half-nodes of the outermost boundary cell. As in the continuous case, these boundary conditions prevent resonances by making the spectrum of the AP complex. Therefore, the overall discrete AP (5a–5d) has a unique solution $u_{m,n}$, $m = 0, \ldots, M$, $n = 0, \ldots, M$, for any right-hand side $\tilde{g}_{m,n}$ defined on the interior sub-grid $m = 1, \ldots, M-1$, $n = 1, \ldots, M-1$. is also It can be solved by a sine FFT in the y direction combined with tri-diagonal elimination in the x direction.[1] The computational complexity of this solution is $\mathcal{O}(M^2 \log M)$ floating point operations.

Next, let the uniform Cartesian grid on the square Ω_0 be denoted by $\mathbb{N}_0$:

$$\mathbb{N}_0 = \left\{(x_m, y_n) \,\middle|\, x_m = mh,\ y_n = nh,\ m = 0, \ldots, M,\ n = 0, \ldots, M\right\}.$$

Creating a discrete analogue of the boundary curve Γ is central to our method since Γ is not aligned with the Cartesian grid. The following subsets of the Cartesian grid $\mathbb{N}_0$ are used for that purpose. Let $\mathbb{M}_0 \subset \mathbb{N}_0$ be the set of only interior nodes of the square domain Ω_0, i.e., $\mathbb{M}_0$ contains all nodes of $\mathbb{N}_0$ except for those along the boundary edges of the square:

$$\mathbb{M}_0 = \left\{(x_m, y_n) \,\middle|\, x_m = mh,\ y_n = nh,\ m = 1, \ldots, M-1,\ n = 1, \ldots, M-1\right\}.$$

Notice that if we were to form a set which contains all of the nodes "touched" by the 9-point compact stencil operating on the set $\mathbb{M}_0$, that this set would coincide exactly with $\mathbb{N}_0$, and it is for this reason that the right-hand side $g_{m,n}$ of the discrete AP (5a–5d) is defined only on the interior nodes, i.e., on $\mathbb{M}_0$. We now distinguish those nodes which are inside the boundary curve Γ from those which are outside Γ. Let all of those nodes which are confined within the continuous boundary Γ, i.e., the unit circle, be denoted by $\mathbb{M}^+ \subset \mathbb{M}_0$, and those which are outside, except for the edges of the auxiliary domain, by $\mathbb{M}^- \subset \mathbb{M}_0$. Next, let the collections of all nodes touched by the 9-point compact stencil operating on the nodes of $\mathbb{M}^+$ and $\mathbb{M}^-$ be referred to as $\mathbb{N}^+$ and $\mathbb{N}^-$, respectively. Then, there will be a nonempty intersection in the sets $\mathbb{N}^+$ and $\mathbb{N}^-$, and this is what we refer to as the grid boundary: $\gamma = \mathbb{N}^+ \cap \mathbb{N}^-$. All the foregoing grid sets are visualized in Fig. 1.

1.4. Difference potentials

The AP (5a–5d) plays a vital role in the construction of difference potentials and projections [15]. The difference potential can be thought of as a discrete analogue to Calderon's potentials [5,16], and it will approximate the solution u of boundary value problem (2a–2b) on the grid $\mathbb{N}^+$. Accordingly, the difference projection is a discrete counterpart of Calderon's boundary projections. The density of the potential that approximates the solution u must satisfy the special boundary equation with projection (BEP), see formula (8) below. In this section, we provide only a very brief account of difference potentials and projections, while subsequent detail can be found in [15,13,14].

Let $\boldsymbol{L}^{(h)}$ denote the 9-point finite difference operator on the left-hand side of Eq. (5a). The overall discrete AP (5a–5d) is stated as the solution of $\boldsymbol{L}^{(h)}u = \tilde{g}$ on the grid $\mathbb{N}_0$ subject to boundary conditions (5b), (5c), and (5d). Let $\boldsymbol{G}^{(h)}$ denote the

[1] Numerical stability of the discrete AP (5a–5d) and, in particular, its dependence on the wavenumber k, has not been studied theoretically. In our simulations, see Section 4, we have not observed any indication of instability.

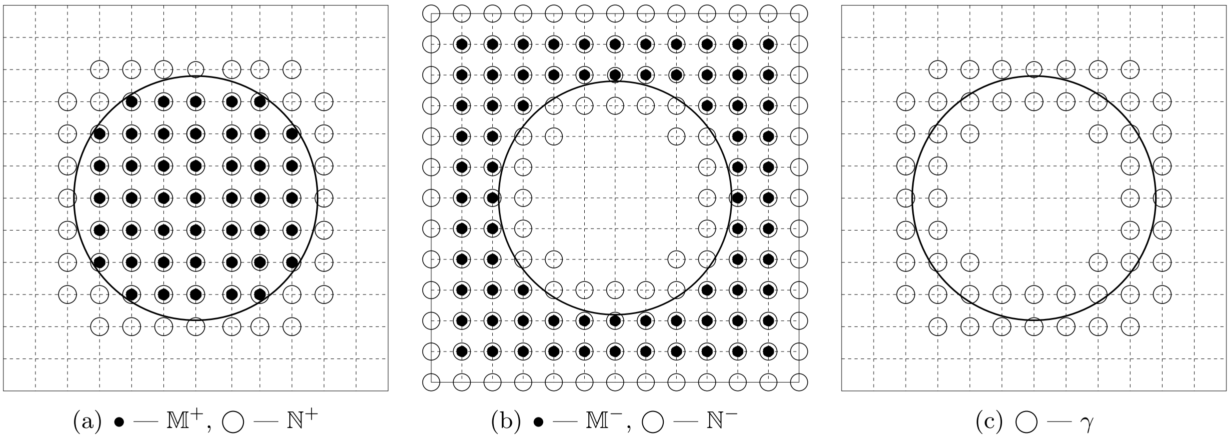

Fig. 1. Interior and exterior grid subsets and the grid boundary.

corresponding inverse operator to $\boldsymbol{L}^{(h)}$, so that the solution to the discrete AP (5a–5d) is given by $u = \boldsymbol{G}^{(h)}\tilde{g}$. Next, let ξ_γ be a grid function specified on the discrete boundary γ, see Fig. 1(c). Then, the difference potential with density ξ_γ is defined on the grid set $\mathbb{N}^+ \subset \mathbb{N}_0$ as follows:

$$\boldsymbol{P}_{\mathbb{N}^+}\xi_\gamma \stackrel{\text{def}}{=} w - \boldsymbol{G}^{(h)} \underbrace{\left(\boldsymbol{L}^{(h)} w|_{\mathbb{M}^+}\right)}_{\tilde{g}}, \quad \text{where } w = \begin{cases} \xi_\gamma & \text{on } \gamma, \\ 0 & \text{on } \mathbb{N}_0 \backslash \gamma. \end{cases} \tag{6}$$

In formula (6), the operation $\boldsymbol{L}^{(h)} w|_{\mathbb{M}^+}$ means that the operator $\boldsymbol{L}^{(h)}$ is first applied to the auxiliary function w, and then the grid function $\boldsymbol{L}^{(h)} w$ is truncated to the grid $\mathbb{M}^+$, see Fig. 1(a). The difference potential $\boldsymbol{P}_{\mathbb{N}^+}\xi_\gamma$ maps a function ξ_γ defined on the grid boundary $\gamma \subset \mathbb{N}^+$ to a function defined on the set $\mathbb{N}^+ \subset \mathbb{N}_0$. For any ξ_γ, it satisfies the homogeneous finite difference equation at the nodes $\mathbb{M}^+$:

$$\boldsymbol{L}^{(h)}(\boldsymbol{P}_{\mathbb{N}^+}\xi_\gamma) = 0.$$

Truncation of the difference potential (6) to γ yields the difference projection:

$$\boldsymbol{P}_\gamma \xi_\gamma \stackrel{\text{def}}{=} (\boldsymbol{P}_{\mathbb{N}^+}\xi_\gamma)|_\gamma. \tag{7}$$

As shown in [15], a given grid function ξ_γ coincides on γ with a solution u to the finite difference equation (3): $\boldsymbol{L}^{(h)} u = \tilde{f}$ [where u is defined on $\mathbb{N}^+$, Fig. 1(a)] if and only if it satisfies the BEP:

$$\boldsymbol{P}_\gamma \xi_\gamma + \boldsymbol{TrG}^{(h)} \tilde{f} = \xi_\gamma, \tag{8}$$

where $\boldsymbol{TrG}^{(h)} \tilde{f}$ denotes the trace on the grid boundary γ of a grid function $\boldsymbol{G}^{(h)} \tilde{f}$ defined on $\mathbb{N}_0$. In other words, the BEP (8) provides an equivalent reduction of the finite difference equation $\boldsymbol{L}^{(h)} u = \tilde{f}$ from the grid domain $\mathbb{N}^+$ to the grid boundary γ. This is the key property that we wish to exploit. Our method will rely on solving the BEP (8) for ξ_γ, while the boundary conditions will be taken into account as described in Section 1.5. Then, the grid function

$$u = \boldsymbol{P}_{\mathbb{N}^+}\xi_\gamma + \boldsymbol{G}^{(h)} \tilde{f}, \tag{9}$$

where the difference potential is given by (6), will approximate the solution to the BVP (2a–2b).

One may observe that the choice of the AP affects the definition of both the difference potential (6) and the projection (7) since the inverse operator $\boldsymbol{G}^{(h)}$ corresponds to the specified AP (5a–5d). We emphasize though that changing the AP, under the constraint that it still has a unique solution, does not change the range of the projection $\boldsymbol{P}_\gamma$, and, consequently, does not change the set of solutions to the BEP (8) either. In other words, when changing the AP one changes only the projection angle onto the same subspace, see [15].

1.5. Boundary conditions

We now describe our general method for dealing with the given boundary condition (2b) of the BVP. This begins with the equation-based extension of a pair of functions $\boldsymbol{\xi}_\Gamma = (\xi_0, \xi_1)$ defined on the continuous boundary, Γ, to a function ξ_γ defined on the discrete boundary, γ. It is precisely this extension that ultimately enables the difference potential to approximate the continuous Calderon potential. Consider $\boldsymbol{\xi}_\Gamma$ as the Cauchy data of some function $v = v(x, y)$,

$$(\xi_0, \xi_1)|_\Gamma = \left(v, \frac{\partial v}{\partial \boldsymbol{n}}\right)\bigg|_\Gamma,$$

that we define near the curve Γ by means of the truncated Taylor expansion:

$$v \stackrel{\text{def}}{=} v_\Gamma + \rho \frac{\partial v}{\partial \boldsymbol{n}}\bigg|_\Gamma + \frac{\rho^2}{2}\frac{\partial^2 v}{\partial \boldsymbol{n}^2}\bigg|_\Gamma + \frac{\rho^3}{6}\frac{\partial^3 v}{\partial \boldsymbol{n}^3}\bigg|_\Gamma + \frac{\rho^4}{24}\frac{\partial^4 v}{\partial \boldsymbol{n}^4}\bigg|_\Gamma. \tag{10}$$

In formula (10), ρ denotes the (signed) distance from a given point near Γ, at which we wish to calculate our new function v, to the curve Γ. We emphasize that while expression (10) has the form of a Taylor approximation to the function v, this is not the case. We are, in fact, defining v at points near Γ whereas originally we are given only v and $\frac{\partial v}{\partial \boldsymbol{n}}$ on Γ. In particular, we call this new function $v = \xi_\gamma$ when it is evaluated at the nodes of the grid boundary γ, see Fig. 1(c):

$$\xi_\gamma \stackrel{\text{def}}{=} v|_\gamma. \tag{11}$$

Of course, to make the definition (10) of the new function v complete, we need to specify the higher order derivatives, whereas thus far we have assumed knowledge of only v and $\frac{\partial v}{\partial \boldsymbol{n}}$ on Γ. Assume that v and $\frac{\partial v}{\partial \boldsymbol{n}}$ are differentiable functions of the polar angle θ on the circle Γ. Also notice that, due to our particular choice of Γ,[2] the normal direction $\boldsymbol{n}$ to the curve coincides with the polar radius r. Then, it becomes useful to write the Helmholtz equation (2a) in polar coordinates:

$$\frac{1}{r}\frac{\partial v}{\partial r} + \frac{\partial^2 v}{\partial r^2} + \frac{1}{r^2}\frac{\partial^2 v}{\partial \theta^2} + k^2 v = f. \tag{12}$$

The desired higher order normal derivatives $\frac{\partial^2 v}{\partial \boldsymbol{n}^2}$, $\frac{\partial^3 v}{\partial \boldsymbol{n}^3}$, and $\frac{\partial^4 v}{\partial \boldsymbol{n}^4}$ for formula (10) will be obtained with the help of Eq. (12). First, we solve (12) for $\frac{\partial^2 v}{\partial \boldsymbol{n}^2}$ as follows:

$$\frac{\partial^2 v}{\partial r^2} = -\left(\frac{1}{r}\frac{\partial v}{\partial r} + \frac{1}{r^2}\frac{\partial^2 v}{\partial \theta^2} + k^2 v\right) + f. \tag{13}$$

Note that the term $\frac{\partial^2 v}{\partial \theta^2}$ in (13) is computed analytically since it is a tangential derivative of v. We then differentiate expression (13) twice with respect to r to obtain the remaining normal derivatives:

$$\frac{\partial^3 v}{\partial r^3} = \frac{1}{r^2}\frac{\partial v}{\partial r} - \frac{1}{r}\frac{\partial^2 v}{\partial r^2} + \frac{2}{r^3}\frac{\partial^2 v}{\partial \theta^2} - \frac{1}{r^2}\frac{\partial^3 v}{\partial r \partial \theta^2} - k^2\frac{\partial v}{\partial r} + \frac{\partial f}{\partial r}, \tag{14}$$

$$\frac{\partial^4 v}{\partial r^4} = -\frac{2}{r^3}\frac{\partial v}{\partial r} + \frac{2}{r^2}\frac{\partial^2 v}{\partial r^2} - \frac{1}{r}\frac{\partial^3 v}{\partial r^3} - \frac{6}{r^4}\frac{\partial^2 v}{\partial \theta^2} + \frac{4}{r^3}\frac{\partial^3 v}{\partial r \partial \theta^2} - \frac{1}{r^2}\frac{\partial^4 v}{\partial r^2 \partial \theta^2} - k^2\frac{\partial^2 v}{\partial r^2} + \frac{\partial^2 f}{\partial r^2}. \tag{15}$$

Notice again that all of the terms which are θ derivatives of v and $\frac{\partial v}{\partial r}$ can be computed analytically. This leaves only the term $\frac{\partial^4 v}{\partial r^2 \partial \theta^2}$ which has not been accounted for, and we obtain it by differentiating (13) twice with respect to θ:

$$\frac{\partial^4 v}{\partial r^2 \partial \theta^2} = -\left(\frac{1}{r}\frac{\partial^3 v}{\partial r \partial \theta^2} + \frac{1}{r^2}\frac{\partial^4 v}{\partial \theta^4} + k^2\frac{\partial^2 v}{\partial \theta^2}\right) + \frac{\partial^2 f}{\partial \theta^2}. \tag{16}$$

Again, all terms needed to compute $\frac{\partial^4 v}{\partial r^2 \partial \theta^2}$ via (16) are known since they are tangential derivatives of v or of $\frac{\partial v}{\partial r}$. Additionally, all of the derivatives of f which appear in (13–16) are assumed to be known, and thus we are able to effectively compute all terms of the expansion (10) via the expressions (13–16) for the normal derivatives.

It will be convenient for us to single out the contribution of the right-hand side f of (12) to formula (10) or, equivalently, decouple expressions (13–16) into the homogeneous part and inhomogeneous part. To do so, we will compute the normal derivatives (13–16) of v as if they were obtained from the homogeneous Helmholtz equation:

$$\begin{aligned}
\frac{\partial^2 v}{\partial r^2} &= -\left(\frac{1}{r}\frac{\partial v}{\partial r} + \frac{1}{r^2}\frac{\partial^2 v}{\partial \theta^2} + k^2 v\right),\\
\frac{\partial^3 v}{\partial r^3} &= \frac{1}{r^2}\frac{\partial v}{\partial r} - \frac{1}{r}\frac{\partial^2 v}{\partial r^2} + \frac{2}{r^3}\frac{\partial^2 v}{\partial \theta^2} - \frac{1}{r^2}\frac{\partial^3 v}{\partial r \partial \theta^2} - k^2\frac{\partial v}{\partial r},\\
\frac{\partial^4 v}{\partial r^4} &= -\frac{2}{r^3}\frac{\partial v}{\partial r} + \frac{2}{r^2}\frac{\partial^2 v}{\partial r^2} - \frac{1}{r}\frac{\partial^3 v}{\partial r^3} - \frac{6}{r^4}\frac{\partial^2 v}{\partial \theta^2} + \frac{4}{r^3}\frac{\partial^3 v}{\partial r \partial \theta^2} - \frac{1}{r^2}\frac{\partial^4 v}{\partial r^2 \partial \theta^2} - k^2\frac{\partial^2 v}{\partial r^2},\\
\frac{\partial^4 v}{\partial r^2 \partial \theta^2} &= -\left(\frac{1}{r}\frac{\partial^3 v}{\partial r \partial \theta^2} + \frac{1}{r^2}\frac{\partial^4 v}{\partial \theta^4} + k^2\frac{\partial^2 v}{\partial \theta^2}\right),
\end{aligned} \tag{17}$$

and then separately collect the inhomogeneous terms of Eqs. (13–16). In doing so, the Taylor expansion (10) is decomposed into the homogeneous and inhomogeneous contribution as follows:

[2] A similar development, but for a general smooth curve rather than only for a circle, is presented in [13].

$$\begin{aligned} v = &\underbrace{v_\Gamma + \rho \frac{\partial v}{\partial r}\bigg|_\Gamma + \frac{\rho^2}{2}\frac{\partial^2 v}{\partial r^2}\bigg|_\Gamma + \frac{\rho^3}{6}\frac{\partial^3 v}{\partial r^3}\bigg|_\Gamma + \frac{\rho^4}{24}\frac{\partial^4 v}{\partial r^4}\bigg|_\Gamma}_{\text{homogeneous}} \\ &+ \underbrace{\frac{\rho^2}{2} f + \frac{\rho^3}{6}\left(\frac{\partial f}{\partial r} - \frac{1}{r} f\right) + \frac{\rho^4}{24}\left(\frac{\partial^2 f}{\partial r^2} - \frac{1}{r^2}\frac{\partial^2 f}{\partial \theta^2} - \frac{1}{r}\frac{\partial f}{\partial r} - k^2 f + \frac{3}{r^2} f\right)}_{\text{inhomogeneous}}. \end{aligned} \tag{18}$$

The derivatives of v w.r.t. r in formula (18) are computed according to the homogeneous expressions (17). One advantage of decomposition (18) is that it reduces redundant computations: observe that the inhomogeneous contribution contains no terms which are associated with the input functions $\boldsymbol{\xi}_\Gamma = (\xi_0, \xi_1) = (v, \frac{\partial v}{\partial \boldsymbol{n}})|_\Gamma$, and thus we may calculate this portion of the extension once and for all.

In the case that $\boldsymbol{\xi}_\Gamma = (\xi_0, \xi_1)$ happens to be the trace of a function v which satisfies the inhomogeneous Helmholtz equation (2a) on Ω, i.e., $\xi_0 = v|_\Gamma$ and $\xi_1 = \frac{\partial v}{\partial \boldsymbol{n}}|_\Gamma$, then formula (10) or, equivalently, (18), yields a fifth order Taylor approximation of v. We emphasize, however, that these formulae can be applied to any function $\boldsymbol{\xi}_\Gamma = (\xi_0, \xi_1)$ given at the boundary Γ, and we will actually apply them to the specially chosen basis functions which are not traces of any solution to the Helmholtz equation. This will allow us to incorporate the boundary condition (2b) into the discrete BEP (8). To that end, we will consider the extension process defined by (18) as an affine transformation $\boldsymbol{Ex}$, which maps a pair of functions $\xi_\Gamma = (\xi_0, \xi_1)|_\Gamma$ defined on the circle Γ to a new function ξ_γ defined at the nodes of the discrete boundary γ:

$$\xi_\gamma = \boldsymbol{Ex}\boldsymbol{\xi}_\Gamma = \boldsymbol{Ex}(\xi_0, \xi_1)|_\Gamma = \boldsymbol{Ex}_H(\xi_0, \xi_1)|_\Gamma + \boldsymbol{Ex}_I f, \tag{19}$$

where $\boldsymbol{Ex}_H$ and $\boldsymbol{Ex}_I$ are the homogeneous and inhomogeneous contribution of (18), respectively. Note that while $\boldsymbol{Ex}$ is an affine mapping, $\boldsymbol{Ex}_H$ is a linear operator w.r.t. its argument $\boldsymbol{\xi}_\Gamma$.

The functions that we are going to apply the extension mapping $\boldsymbol{Ex}$ to will form a basis on the boundary Γ, with respect to which the Cauchy data of the solution can be expanded. Then, by extending the basis functions according to (19) and incorporating the boundary data given in (2b), we establish a linear system for the coefficients of the basis expansion via the BEP (8). Having solved this system, we can reconstruct ξ_γ and finally approximate the solution that we seek in the form (9). Therefore, we now describe in general the basis and the linear system for the coefficients, followed by our specific choice of basis functions.

Consider a set of orthogonal basis functions ψ_n, $n = 0, \dots, N$, defined on Γ. For simplicity, we will employ both the same type and number of basis functions for both the Dirichlet and Neumann data, but in general this is not required. We seek an expansion of a given $\boldsymbol{\xi}_\Gamma$ in the form

$$\boldsymbol{\xi}_\Gamma = (\xi_0, \xi_1)|_\Gamma = \underbrace{\sum_{n=0}^{N} c_n^{(0)}(\psi_n, 0)}_{(\xi_0, 0)} + \underbrace{\sum_{n=0}^{N} c_n^{(1)}(0, \psi_n)}_{(0, \xi_1)}, \tag{20}$$

where $c_n^{(0)}$ and $c_n^{(1)}$ are the coefficients. For typical problems solved by difference potentials, we use rapidly converging expansions (20), such as Fourier or Chebyshev, that can be truncated at relatively low values of N, see [4,13,14]. Specific implementation details, including basis dimensions, for the algorithm of the current paper are provided in Section 4.

We will abbreviate the notation of the basis functions $(\psi_n, 0)$ and $(0, \psi_n)$ by $\boldsymbol{\psi}_n^{(0)}$ and $\boldsymbol{\psi}_n^{(1)}$. In order to implement the BEP (8), we first form the grid function ξ_γ by applying the extension mapping (19) to the expansion (20):

$$\xi_\gamma = \boldsymbol{Ex}\boldsymbol{\xi}_\Gamma = \boldsymbol{Ex}\left(\sum_{n=0}^{N} c_n^{(0)}\boldsymbol{\psi}_n^{(0)} + \sum_{n=0}^{N} c_n^{(1)}\boldsymbol{\psi}_n^{(1)}\right) = \sum_{n=0}^{N} c_n^{(0)}\boldsymbol{Ex}_H\,\boldsymbol{\psi}_n^{(0)} + \sum_{n=0}^{N} c_n^{(1)}\boldsymbol{Ex}_H\,\boldsymbol{\psi}_n^{(1)} + \boldsymbol{Ex}_I f. \tag{21}$$

Then, we substitute the representation (21) into the BEP (8) to obtain a system of linear equations for the coefficients $c_n^{(0)}$ and $c_n^{(1)}$:

$$\sum_{n=0}^{N} c_n^{(0)}\boldsymbol{P}_\gamma\boldsymbol{Ex}_H\,\boldsymbol{\psi}_n^{(0)} + \sum_{n=0}^{N} c_n^{(1)}\boldsymbol{P}_\gamma\boldsymbol{Ex}_H\,\boldsymbol{\psi}_n^{(1)} + \boldsymbol{P}_\gamma\boldsymbol{Ex}_I f + \boldsymbol{TrG}^{(h)}\tilde{f} = \sum_{n=0}^{N} c_n^{(0)}\boldsymbol{Ex}_H\,\boldsymbol{\psi}_n^{(0)} + \sum_{n=0}^{N} c_n^{(1)}\boldsymbol{Ex}_H\,\boldsymbol{\psi}_n^{(1)} + \boldsymbol{Ex}_I f.$$

We simplify this expression by gathering the corresponding basis terms on the left-hand side:

$$\sum_{n=0}^{N} c_n^{(0)}(\boldsymbol{P}_\gamma - \boldsymbol{I}_\gamma)\boldsymbol{Ex}_H\,\boldsymbol{\psi}_n^{(0)} + \sum_{n=0}^{N} c_n^{(1)}(\boldsymbol{P}_\gamma - \boldsymbol{I}_\gamma)\boldsymbol{Ex}_H\,\boldsymbol{\psi}_n^{(1)} = -\boldsymbol{TrG}^{(h)}\tilde{f} - (\boldsymbol{P}_\gamma - \boldsymbol{I}_\gamma)\boldsymbol{Ex}_I f, \tag{22}$$

where $\boldsymbol{I}_\gamma$ is the identity operator in the space of grid functions ξ_γ defined on γ. In matrix form, the linear system (22) can be recast as

$$\boldsymbol{Q}_H \boldsymbol{c} = -\boldsymbol{TrG}^{(h)} \tilde{f} - (\boldsymbol{P}_\gamma - \boldsymbol{I}_\gamma)\boldsymbol{Ex}_I f, \tag{23}$$

in which the first $N+1$ columns of the matrix $\boldsymbol{Q}_H$ are given by $(\boldsymbol{P}_\gamma - \boldsymbol{I}_\gamma)\boldsymbol{Ex}_H \boldsymbol{\psi}_n^{(0)}$ for $n = 0, \dots, N$ and the second $N+1$ columns by $(\boldsymbol{P}_\gamma - \boldsymbol{I}_\gamma)\boldsymbol{Ex}_H \boldsymbol{\psi}_n^{(1)}$ for $n = 0, \dots, N$. Accordingly, $\boldsymbol{c}$ is the vector of dimension $2(N+1)$, with the first $N+1$ components of $\boldsymbol{c}$ being the coefficients $c_n^{(0)}$, $n = 0, \dots, N$, that pertain to the Dirichlet data, and the second $N+1$ components being the coefficients $c_n^{(1)}$, $n = 0, \dots, N$, that pertain to the Neumann data:

$$\boldsymbol{c} = \left[\boldsymbol{c}^{(0)}, \boldsymbol{c}^{(1)}\right]^T = \left[c_0^{(0)}, \dots, c_N^{(0)}, c_0^{(1)}, \dots, c_N^{(1)}\right]^T. \tag{24}$$

Similarly, we partition the matrix $\boldsymbol{Q}_H$ into the Dirichlet and Neumann sub-matrices:

$$\begin{aligned} \boldsymbol{Q}_H &= \left[\boldsymbol{Q}^{(0)}, \boldsymbol{Q}^{(1)}\right] \\ &= \left[(\boldsymbol{P}_\gamma - \boldsymbol{I}_\gamma)\boldsymbol{Ex}_H \boldsymbol{\psi}_0^{(0)}, \dots, (\boldsymbol{P}_\gamma - \boldsymbol{I}_\gamma)\boldsymbol{Ex}_H \boldsymbol{\psi}_N^{(0)}, (\boldsymbol{P}_\gamma - \boldsymbol{I}_\gamma)\boldsymbol{Ex}_H \boldsymbol{\psi}_0^{(1)}, \dots, (\boldsymbol{P}_\gamma - \boldsymbol{I}_\gamma)\boldsymbol{Ex}_H \boldsymbol{\psi}_N^{(1)}\right]. \end{aligned} \tag{25}$$

The dimension of the matrix $\boldsymbol{Q}_H$ of (25) is $|\gamma| \times 2(N+1)$, where $|\gamma|$ is the number of nodes in the grid boundary γ and $2(N+1)$ in the expansion (20). The right-hand side of system (23) is a vector of dimension $|\gamma|$, which is due to the right-hand side f of the differential equation (2a). Then, introducing a new, shorter, notation $\boldsymbol{Q}_I f = (\boldsymbol{P}_\gamma - \boldsymbol{I}_\gamma)\boldsymbol{Ex}_I f$, we recast system (25) as follows:

$$\boldsymbol{Q}_H \boldsymbol{c} = -\boldsymbol{TrG}^{(h)} \tilde{f} - \boldsymbol{Q}_I f. \tag{26}$$

In actual numerical simulations (see Section 4), we normally have $|\gamma| > 2(N+1)$, or even $|\gamma| \gg 2(N+1)$ on fine grids, because the number of basis functions N is fixed at a relatively low value that already enables sufficient accuracy at the boundary, whereas the grid is refined to obtain a better accuracy inside the domain (as well as to demonstrate convergence). Then, the set of linear equations (26) forms an overdetermined system of $|\gamma|$ equations with respect to $2(N+1)$ unknowns. After taking into account the boundary condition (2b), this system is solved in the sense of least squares.

For example, if the given boundary condition (2b) is of Dirichlet type, $u|_\Gamma = \phi(\theta)$, then the coefficients $\{c_n^{(0)}\}_{n=0}^N$ can be readily computed and considered known. We then precompute the product $\boldsymbol{Q}^{(0)}\boldsymbol{c}^{(0)}$ and solve the rest of system (26) for the remaining coefficients $\{\boldsymbol{c}_n^{(1)}\}_{n=0}^N$ by least squares:

$$\boldsymbol{Q}^{(1)}\boldsymbol{c}^{(1)} = -\boldsymbol{TrG}^{(h)} \tilde{f} - \boldsymbol{Q}_I f - \boldsymbol{Q}^{(0)}\boldsymbol{c}^{(0)}. \tag{27}$$

The same can be done if the boundary condition (2b) of the BVP is of Neumann type. In this case, we expand the Neumann data, pre-multiply, and subtract as before to form the system

$$\boldsymbol{Q}^{(0)}\boldsymbol{c}^{(0)} = -\boldsymbol{TrG}^{(h)} \tilde{f} - \boldsymbol{Q}_I f - \boldsymbol{Q}^{(1)}\boldsymbol{c}^{(1)}, \tag{28}$$

that is solved for the coefficients $\{c_j^{(0)}\}_{j=0}^N$ of the Dirichlet data by least squares.

Next, we introduce our particular choice of basis functions, the Chebyshev polynomials $\{T_n(x)\}_{n=0}^\infty$. They are orthogonal on $x \in [-1, 1]$ with the weight $\omega(x) = 2/\pi\sqrt{1-x^2}$. For an r times continuously differentiable function $\phi(x)$, $\phi(x) \in C^r[-1, 1]$, such that $\phi^{(r+1)}(x) \in L_2[-1, 1]$, its Chebyshev expansion on the interval $[-1, 1]$:

$$\phi(x) = \sum_{n=0}^N \hat{\phi}_n T_n(x), \quad \text{where } \hat{\phi}_n = \begin{cases} \frac{1}{2}\int_{-1}^1 \omega(x)\phi(x)T_n(x)dx, & n = 0, \\ \int_{-1}^1 \omega(x)\phi(x)T_n(x)dx, & n > 0, \end{cases} \tag{29}$$

converges with the rate $o(N^{-(r+\frac{1}{2})})$. For an infinitely smooth $\phi(x)$, the convergence is spectral.

A convenient aspect of the Chebyshev basis is the capability to expand non-periodic functions. Therefore, we may partition the circle Γ into any number of segments and use an independent Chebyshev system for each segment, and this proves very efficient for setting mixed and/or discontinuous boundary conditions, see [4]. In the current paper, we will partition Γ into the upper and lower semicircles, $\Gamma_1 = \{(r, \theta) | r = 1, \theta \in [0, \pi)\}$ and $\Gamma_2 = \{(r, \theta) | r = 1, \theta \in [\pi, 2\pi)\}$, and allow for jump discontinuities of the boundary data at the points $\theta = 0$ and $\theta = \pi$.

To build Chebyshev expansions for the functions defined on the upper and lower semicircles, one needs to obtain Chebyshev polynomials of the arguments $\theta \in [0, \pi)$ and $\theta \in [\pi, 2\pi)$. To do so, one would typically use a linear change of variables to map each of these subintervals onto the interval $x \in [-1, 1)$. However, in order to avoid numerical difficulties which arise from computing the derivatives[3] of the Chebyshev functions near the endpoints $x = -1$ and $x = 1$, we will instead map these subintervals onto a slightly smaller domain, $x \in [-1 + \varepsilon, 1 - \varepsilon)$, where $\varepsilon > 0$. The corresponding mappings for the upper and lower semicircles, are given by

[3] Tangential derivatives are needed when building the extension $\boldsymbol{Ex}$ using (17), see [4] for a detailed discussion.

$$x = \left(\frac{\theta}{\pi} + \frac{\theta - \pi}{\pi}\right)(1 - \varepsilon) \tag{30a}$$

and

$$x = \left(\frac{\theta - \pi}{\pi} + \frac{\theta - 2\pi}{\pi}\right)(1 - \varepsilon), \tag{30b}$$

respectively. Let us now consider, for example, a function $\phi(\theta)$ defined for $\theta \in [0, \pi)$. The inverse mapping of (30a) transforms the interval $x \in [-1, 1)$ into a larger interval $\theta \in [-\pi\sigma, \pi + \pi\sigma) \supset [0, \pi)$, where $\sigma = \frac{1}{2}\frac{\varepsilon}{1-\varepsilon} > 0$. Then, to build the Chebyshev expansion (29) for ϕ, we must first extend ϕ from $\theta \in [0, \pi)$ to this remaining portions of the larger interval, $\theta \in [-\pi\sigma, 0) \cup [\pi, \pi + \pi\sigma)$, or, equivalently, to $x \in [-1, -1 + \varepsilon) \cup [1 - \varepsilon, 1)$. One way of doing that is to use the analytic expression for the function if it is available. Alternatively, we may build a smooth polynomial extension of any desired order from the endpoints $\theta = 0$ and $\theta = \pi$ to $\theta \in [-\pi\sigma, 0)$ and $\theta \in [\pi, \pi + \pi\sigma)$, respectively. The specific form of this extension, however, is not important as long as the desired degree of smoothness that guarantees the desired rate of convergence of (29) is maintained. Indeed, the transformation $\boldsymbol{Ex}$ of (19) is going to be applied only to the Chebyshev basis functions on the original interval $\theta \in [0, \pi)$ rather than the extended interval $\theta \in [-\pi\sigma, \pi + \pi\sigma)$. In our previous paper [4], we concluded that taking $\epsilon = 0.001$ was sufficient to avoid any undesirable computations near the endpoints of the Chebyshev interval, and this has been confirmed by the numerical results presented there. The considerations for the lower semicircle $\theta \in [\pi, 2\pi)$ and its corresponding mapping (30b) are identical. The end result is that we have an expansion of the following form for a given function $\phi(x)$:

$$\phi(x) = \sum_{n=0}^{N} \hat{\phi}_n T_n(x), \quad x \in [-1 + \varepsilon, 1 - \varepsilon), \tag{31}$$

where the coefficients $\hat{\phi}_n$ are obtained using the function ϕ extended to the larger interval $x \in [-1, 1)$. Since (29) is uniformly convergent on $[-1, 1)$, it is necessarily uniformly convergent on any subinterval, in particular, on $[-1 + \varepsilon, 1 - \varepsilon)$, since, for any given ϕ, the values of the expansions (29) and (31) must coincide on $[-1 + \varepsilon, 1 - \varepsilon)$. Moreover, as has been mentioned, while the behavior of the expansion (31) may vary at the "tails" $[-1, -1 + \varepsilon) \cup [1 - \varepsilon, 1)$ depending on how the function ϕ was extended, this behavior is inconsequential since we never perform computations on these tails.

Let us now see how the partition of the circle Γ into the semicircles Γ_1 and Γ_2 will affect the algorithm as described thus far. First, we will have two double sets of coefficients instead of one (one double set per semicircle), so that formula (24) is replaced by

$$\begin{aligned}
\left[\boldsymbol{c}^{(0,1)}, \boldsymbol{c}^{(1,1)}\right]^T &= \left[c_0^{(0,1)}, \ldots, c_N^{(0,1)}, c_1^{(1,1)}, \ldots, c_N^{(1,1)}\right]^T, \\
\left[\boldsymbol{c}^{(0,2)}, \boldsymbol{c}^{(1,2)}\right]^T &= \left[c_0^{(0,2)}, \ldots, c_N^{(0,2)}, c_1^{(1,2)}, \ldots, c_N^{(1,2)}\right]^T,
\end{aligned} \tag{32}$$

and $\boldsymbol{c} = [\boldsymbol{c}^{(0,1)}, \boldsymbol{c}^{(1,1)}, \boldsymbol{c}^{(0,2)}, \boldsymbol{c}^{(1,2)}]^T$. The form of the expansion (20) of $\boldsymbol{\xi}_\Gamma$ becomes

$$\boldsymbol{\xi}_\Gamma = \underbrace{\sum_{n=0}^{N} c_n^{(0,1)} \boldsymbol{\psi}_n^{(0,1)} + \sum_{n=0}^{N} c_n^{(0,2)} \boldsymbol{\psi}_n^{(0,2)}}_{(\xi_0, 0)} + \underbrace{\sum_{n=0}^{N} c_n^{(1,1)} \boldsymbol{\psi}_n^{(1,1)} + \sum_{n=0}^{N} c_n^{(1,2)} \boldsymbol{\psi}_n^{(1,2)}}_{(0, \xi_1)},$$

where

$$\begin{aligned}
\boldsymbol{\psi}_n^{(0,1)} &= \begin{cases} (T_n, 0) & \text{on } \Gamma_1, \\ (0, 0) & \text{on } \Gamma_2, \end{cases} &\quad \boldsymbol{\psi}_n^{(0,2)} &= \begin{cases} (0, 0) & \text{on } \Gamma_1, \\ (T_n, 0) & \text{on } \Gamma_2, \end{cases} \\
\boldsymbol{\psi}_n^{(1,1)} &= \begin{cases} (0, T_n) & \text{on } \Gamma_1, \\ (0, 0) & \text{on } \Gamma_2, \end{cases} &\quad \boldsymbol{\psi}_n^{(1,2)} &= \begin{cases} (0, 0) & \text{on } \Gamma_1, \\ (0, T_n) & \text{on } \Gamma_2. \end{cases}
\end{aligned} \tag{33}$$

The extension of a given basis function (33) from Γ to γ is then computed by the same formulae (17–18) as before. The matrix $\boldsymbol{Q}_H$ of (25) is now partitioned into two sets of two blocks, one set for each segment of the boundary, and will have the overall dimension $|\gamma| \times [2(N+1) + 2(N+1)]$:

$$\boldsymbol{Q}_H = \left[\boldsymbol{Q}_0^{(1)} \quad \boldsymbol{Q}_1^{(1)} \quad \boldsymbol{Q}_0^{(2)} \quad \boldsymbol{Q}_1^{(2)}\right]. \tag{34}$$

The partition $\Gamma = \Gamma_1 \cup \Gamma_2$ will allow us to consider discontinuous boundary data, as discussed in the remainder of the paper; however, this partition allows for even more than that. In particular, one can take into account a mixed boundary condition, e.g., of the Dirichlet/Neumann type. We have conducted the corresponding simulations in [4], and here we only provide a brief example. If, say, the boundary condition (2b) is given by $u|_{\Gamma_1} = \phi(\theta), \theta \in [0, \pi)$, and $\frac{\partial u}{\partial \boldsymbol{n}}|_{\Gamma_2} = \lambda(\theta), \theta \in [\pi, 2\pi)$, then we may proceed similarly to what we did in formulae (27) and (28), by multiplying $\boldsymbol{Q}_0^{(1)}$ and $\boldsymbol{Q}_1^{(2)}$ by the known coefficients $\{\boldsymbol{c}_n^{(0,1)}\}_{n=0}^N$ and $\{\boldsymbol{c}_n^{(1,2)}\}_{n=0}^N$ to form the system

$$\left[\boldsymbol{Q}_1^{(1)}\ \boldsymbol{Q}_0^{(2)}\right]\left[\boldsymbol{c}^{(1,1)}\ \boldsymbol{c}^{(0,2)}\right]^T = -\boldsymbol{TrG}^{(h)}\tilde{f} - \boldsymbol{Q}_I f - \boldsymbol{Q}_0^{(1)}\boldsymbol{c}^{(0,1)} - \boldsymbol{Q}_1^{(2)}\boldsymbol{c}^{(1,2)},$$

which is then solved in the sense of least squares.

2. Near-boundary singularities

In Sections 1.3 through 1.5, we have shown how to solve the regularized BVP (2a–2b) by the method of difference potentials. In this section, we will show how to transition from the original BVP (1a–1b) for which the solution u may have singularities, to the new BVP (2a–2b), for which the solution is sufficiently smooth so that it can be approximated by means of a high order accurate scheme. For definiteness, we will first analyze the case of a Dirichlet boundary condition (1b) in problem (1a–1b) $\boldsymbol{l}_\Gamma = 1$. The Neumann and mixed cases are treated similarly, and in Sections 3 and 4 we present the setup and the results of computations for both Dirichlet and Neumann boundary conditions.

We allow the function $\phi_\Gamma(s)$ on the right-hand side of (1b) and/or its derivatives to have jump discontinuities at some locations on the boundary Γ. In addition, we allow the boundary Γ itself to have corners, i.e., be only piecewise smooth. Discontinuities of either type generally reduce the regularity of the solution in the vicinity of the corresponding boundary points, as some derivatives of the solution become unbounded. This, in turn, slows down the convergence of finite difference methods, see [4]. Hereafter, we describe a consistent and general approach to restoring the rate of convergence affected by the reduced regularity of the solution. It exploits an analytically derived asymptotic expansion of the solution near the "irregular" boundary points.

Specifically, let $u_0, u_1, \ldots, u_n$ be the first $n+1$ consecutive terms of an asymptotic expansion of the exact solution u to the BVP (1a–1b) in the vicinity of a singular boundary point $s = s_0$. Suppose that each term u_j of this expansion is more regular than the previous term, u_{j-1}, i.e., that u_j has bounded derivatives up to a certain order which is higher than the order of the highest bounded derivative of u_{j-1}. Subtracting the sum of $n+1$ such terms from the exact solution u, we arrive at a new function $v = u - (u_0 + u_1 + \ldots + u_n)$, for which we formulate a new BVP [cf. BVP (2a–2b)]:

$$\begin{cases} \boldsymbol{L}v = -\boldsymbol{L}(u_0 + u_1 + \ldots + u_n), \\ v|_\Gamma = \phi_\Gamma(s) - (u_0 + u_1 + \ldots + u_n)|_\Gamma \end{cases} \tag{35}$$

In general, the right-hand side $-\boldsymbol{L}(u_0 + u_1 + \ldots + u_n)$ in (35) is nonzero because neither the individual terms u_j of the expansion nor their sum are expected to satisfy the homogeneous Helmholtz equation. Our goal is to choose the terms u_j in such a way that the function v will have no singularities up to at least the derivative of order n, in which case problem (35) will be referred to as regularized.

By taking an appropriate value of n, one can make the solution v of the regularized problem (35) sufficiently smooth so that a given finite difference scheme will converge to v with the design rate. Then, by adding the analytically derived sum $(u_0 + u_1 + \ldots + u_n)$ to the computed solution v, one would restore the design order of accuracy for the overall discrete approximation of u.

In the remainder of this section, we derive the asymptotic form of the solution to the Helmholtz equation near the singular points at the boundary. Specifically, in Section 2.1 we follow [7] and solve Eq. (1a) near the vertex of a 2D plane wedge with straight boundaries. We focus on the Dirichlet case and describe the Neumann case more briefly. In Section 2.2, we use a conformal mapping to generalize the results of Section 2.1 for the case of boundaries with nonzero curvature. As an example, in Section 2.3 and Appendix A we consider both Dirichlet and Neumann data when Γ is a unit circle, although our techniques can accommodate more complex geometries as well.

2.1. Straight boundaries

Consider the Helmholtz equation (1a) in polar coordinates centered at the vertex of a 2D wedge with straight sides and angle ω. Let ρ and θ denote the polar radius and polar angle, respectively. Then, Eq. (1a) takes the form

$$\left(\frac{\partial^2}{\partial\rho^2} + \frac{1}{\rho}\frac{\partial}{\partial\rho} + \frac{1}{\rho^2}\frac{\partial^2}{\partial\theta^2} + k^2(\rho,\theta)\right)u(\rho,\theta) = 0. \tag{36}$$

Note though that unlike in (1a), we allow for the spatial variation of the wavenumber k in Eq. (36), because it proves useful for the analysis of curved boundaries in Section 2.2. Indeed, after the conformal mapping that we use to straighten the boundaries, a constant coefficient Helmholtz equation transforms into a variable coefficient Helmholtz equation.

Eq. (36) is supplemented by the boundary conditions on each side of the wedge:

$$u(\rho, 0) = F(\rho), \qquad u(\rho, \omega) = H(\rho). \tag{37}$$

We assume that the data in (37) can be expanded into the power series:

$$F(\rho) = \sum_{j=0}^{\infty} f_j \rho^j, \qquad H(\rho) = \sum_{j=0}^{\infty} h_j \rho^j. \tag{38}$$

In doing so, expansions (38) are not required to match at the vertex of the wedge. In other words, the respective coefficients f_j and h_j in (38) may differ from one another. It is precisely this mismatch between the boundary data that will give rise to the singularities in the solution.

In addition, we assume that a convergent expansion exists for $k^2(\rho,\theta)$ as well:

$$k^2(\rho,\theta)=\sum_{j=0}^{\infty}k_j(\theta)\rho^j. \tag{39}$$

Representations (38) and (39) for the boundary data and the wavenumber, respectively, will be needed for constructing the asymptotic expansion of the solution $u=u(\rho,\theta)$ near the singularity.

Specifically, following [7] we seek an asymptotic expansion of the solution to Eq. (36) near $\rho=0$ in the form of a series:

$$u(\rho,\theta)=\sum_{j=0}^{\infty}\rho^j\big(A_j(\theta)\ln\rho+B_j(\theta)\big). \tag{40}$$

Substituting expansions (39) and (40) into Eq. (36) and requiring that the resulting coefficients in front of all terms ρ^j and $\rho^j\ln\rho$, $j=0,1,2,\dots$, be independently equal to zero, we obtain two systems of second order ODEs for $A_j(\theta)$ and $B_j(\theta)$:

$$\begin{cases} A_0''=0,\\ A_1''+1^2\cdot A_1=0,\\ \vdots\\ A_{m+2}''+(m+2)^2A_{m+2}=-\displaystyle\sum_{j=0}^{m}k_{m-j}A_j, \quad m=0,1,2\dots,\\ A_j(0)=A_j(\omega)=0, \quad j=0,1,2,\dots, \end{cases} \tag{41}$$

$$\begin{cases} B_0''=0,\\ B_1''+1^2\cdot B_1=-2A_1,\\ \vdots\\ B_{m+2}''+(m+2)^2B_{m+2}=-\displaystyle\sum_{j=0}^{m}k_{m-j}B_j-2(m+2)A_{m+2}, \quad m=0,1,2\dots,\\ B_j(0)=f_j, \qquad B_j(\omega)=h_j, \quad j=0,1,2,\dots \end{cases} \tag{42}$$

In formulae (41) and (42), primes denote differentiation with respect to θ, and the boundary conditions for $B_j(\theta)$ at $\theta=0$ and $\theta=\omega$ in (42) are obtained with the help of expansions (38).

Systems (41) and (42) are coupled and should therefore be solved concurrently, with individual equations addressed in the consecutive order starting with those for $A_0(\theta)$, $B_0(\theta)$. Schematically, we represent the solution sequence as follows: $A_0(\theta)\to B_0(\theta)\to A_1(\theta)\to B_1(\theta)\to A_2(\theta)\to B_2(\theta)\to\dots$. At each step of this sequence, $j=0,1,2,\dots$, we solve a Sturm–Liouville problem of the type

$$\begin{cases} \Psi_j''+j^2\Psi_j=\mu_j(\theta),\\ \Psi_j(0)=a_j, \qquad \Psi_j(\omega)=b_j. \end{cases} \tag{43}$$

For system (41), i.e., when $\Psi_j=A_j(\theta)$, the right-hand side $\mu_j(\theta)$ in (43) involves lower order coefficients $A_i(\theta)$, $i<j$, in the form of a convolution with the coefficients $k_j(\theta)$. For system (42), i.e., when $\Psi_j=B_j(\theta)$, the right-hand side $\mu_j(\theta)$ includes both lower order coefficients $B_i(\theta)$, $i<j$, and the coefficient $A_j(\theta)$ of the same order.

Next, we will study the solvability of problem (43). To do so, it will be sufficient to consider only the case $a_j=b_j=0$. Indeed, for system (41) the boundary conditions are homogeneous anyway, and for system (42) they can be easily made homogeneous by subtracting an arbitrary (smooth) function $\tilde{\Psi}_j(\theta)$ from the solution such that $\tilde{\Psi}_j(0)=a_j$, $\tilde{\Psi}_j(\omega)=b_j$, and adjusting the right-hand side accordingly. Hence, the reduction of problem (43) to the case $a_j=b_j=0$ presents no loss of generality. At the same time, it considerably simplifies the analysis and discussion below.

The Fredholm alternative holds for the Sturm–Liouville problem (43) for any given j and $a_j=b_j=0$. It means that one of the following two scenarios transpires:

1. Problem (43) has a unique solution, which takes place if $\omega\neq\pi\frac{l}{j}$, $l=1,2,\dots$. This is a non-resonant case: the Sturm–Liouville operator $L_j\equiv\frac{d^2}{d\theta^2}+j^2$ subject to zero Dirichlet conditions has no non-trivial eigenfunctions; the inverse operator (Green's function) L_j^{-1} exists; and the problem $L_j\Psi_j=\mu_j$, $\Psi_j(0)=\Psi_j(\omega)=0$, can be uniquely solved.

2. The resonant case. At $\omega = \pi \frac{l}{j}$, $l = 1, 2, \dots$, there exists a nonzero eigenfunction of the Sturm–Liouville operator L_j. This eigenfunction is merely $\hat{\Psi}_j(\theta) = \sin(j\theta)$, up to a constant factor. In this case, problem (43) has a solution if and only if the solvability condition holds[4]:

$$\int_0^\omega \mu_j(\theta) \sin j\theta d\theta = 0. \tag{44}$$

The solution is given by

$$\Psi_j(\theta) = C_j \sin j\theta + \frac{1}{j} \int_0^\theta \left\{ \cos j\theta' \sin j\theta - \sin j\theta' \cos j\theta \right\} \mu_j(\theta') d\theta', \tag{45}$$

and is not unique, since the coefficient C_j in front of the eigenfunction $\sin j\theta$ is arbitrary and changing it will violate neither the differential equation nor the zero boundary conditions.

Next, it will be convenient to represent the wedge angle as $\omega = \alpha\pi$, where α may be either a rational number or an irrational number. Let us first assume that α is irrational. Then, problem (43) falls into the first proposition of the Fredholm alternative. The coefficients $A_j(\theta)$ are all identically equal to zero, $A_j(\theta) \equiv 0$, $j = 0, 1, 2 \dots$, since the boundary conditions are zero and the solution is unique. The coefficients $B_j(\theta)$ are uniquely determined and in general are not equal to zero identically due to the nonzero boundary conditions. Consequently, for the angles $\omega = \alpha\pi$ with α irrational, we obtain a regular expansion of the solution with no singular logarithmic terms.

If α is a rational number, i.e., $\alpha = \frac{l}{N}$, where l and N are positive integers with GCF 1, then for those j_k for which $j_k \frac{l}{N}$ is also a positive integer,

$$j_k \frac{l}{N} = c_k \in \mathcal{N}, \tag{46}$$

problem (43) falls into the second proposition of the Fredholm alternative. For these j_k, the coefficients $A_{j_k}(\theta) = C^{(A)}_{j_k} \sin j_k\theta$ are eigenfunctions of L_{j_k}, up to an arbitrary factor $C^{(A)}_{j_k}$. Substituting a given $A_{j_k}(\theta)$ into the right-hand side of Eq. (42) for $B_{j_k}(\theta)$ and applying the solvability condition (44), we obtain an algebraic equation for the constant $C^{(A)}_{j_k}$ that can be uniquely solved.

On the other hand, the coefficient $B_{j_k}(\theta)$ appears only partially determined. While the second term in (45) is defined unambiguously, the first term contains the eigenfunction $\sin j_k\theta$ with an arbitrary constant C_{j_k} in front of it. Therefore, in the case of a rational α we obtain nonzero, uniquely determined coefficients $A_{j_k}(\theta)$ for the singular terms $\rho^{j_k} \ln \rho$, and partially determined coefficients $B_{j_k}(\theta)$ for ρ^{j_k}. The successive solution of the coupled systems (41), (42) can be schematically shown as

$$\begin{tikzcd} A_0(\theta) \arrow[r] & B_0(\theta) \arrow[r] & \dots \arrow[r] & A_j(\theta) \arrow[r] & B_j(\theta) \arrow[r] & \dots \arrow[r] & A_{j_k}(\theta) \arrow[r] & B_{j_k}(\theta) \arrow[l, bend left, "C^{(A)}_{j_k}"] \arrow[r] & \dots . \end{tikzcd} \tag{47}$$

Diagram (47) emphasizes that at each step of the sequence the problem falls into one of the two propositions of the Fredholm alternative and either proceeds straightforwardly in the non-resonant case (like the j-th step in (47)) or makes a back loop in the resonant case (like the j_k-th step).

We can also see from (46) that the first non-zero singular term $A_{j_k}(\theta)\rho^{j_k} \ln \rho$ appears in the series at $j_1 = N$. So, as N increases the expansion becomes more regular because the singularity moves to higher order terms. In the limit $N \to \infty$, $l \to \infty$, the ratio l/N approaches an irrational number as long as it remains finite and irreducible. Therefore, the singularity disappears and we arrive at the case of an irrational α discussed above.

Neumann boundary data and boundary data with fractional exponents In the case of a Neumann problem, the boundary conditions are set for the normal derivatives on the sides of the wedge. For the previously described geometry, this is the same as specifying $\frac{1}{\rho}\frac{\partial u}{\partial \theta}$ at $\theta = 0$ and $\theta = \omega$:

$$\frac{1}{\rho}\frac{\partial u(\rho, 0)}{\partial \theta} = F(\rho) = \sum_{j=0}^{\infty} f_j \rho^j, \qquad \frac{1}{\rho}\frac{\partial u(\rho, \omega)}{\partial \theta} = H(\rho) = \sum_{j=0}^{\infty} h_j \rho^j,$$

[4] To verify this, consider the following chain of equalities: $0 = \int_0^\omega \Psi(\theta) L_j \hat{\Psi}(\theta) d\theta = \int_0^\omega \hat{\Psi}(\theta) L_j \Psi(\theta) d\theta = \int_0^\omega \hat{\Psi}(\theta) \mu_j(\theta) d\theta$, where we have used the integration by parts and taken into account that $L_j \hat{\Psi}(\theta) = 0$ and $L_j \Psi_j = \mu_j$.

or, equivalently,

$$\frac{\partial u(\rho,0)}{\partial\theta}=\rho F(\rho)=\sum_{j=0}^{\infty}f_j\rho^{j+1},\qquad \frac{\partial u(\rho,\omega)}{\partial\theta}=\rho H(\rho)=\sum_{j=0}^{\infty}h_j\rho^{j+1}. \tag{48}$$

Expansions (48) suggest that one can seek a solution in the form of a series

$$u(\rho,\theta)=\sum_{j=0}^{\infty}\rho^{j+1}\big(A_j(\theta)\ln\rho+B_j(\theta)\big) \tag{49}$$

which differs from (40) only in that the respective powers of ρ are increased by one. Expansion (49) yields the systems similar to (41–43), but with different coefficients in the equations and with Neumann boundary conditions in the counterpart of the Sturm–Liouville problem (43). The procedure for solving these coupled systems (for $A_j(\theta)$ and $B_j(\theta)$) remains the same as for the Dirichlet case.

We can also consider a more general class of the boundary data, with expansions that include non-integer powers:

$$F(\rho)=\rho^{\beta}\sum_{j=0}^{\infty}f_j\rho^j,\qquad H(\rho)=\rho^{\gamma}\sum_{j=0}^{\infty}h_j\rho^j,\quad 0<\beta,\gamma<1.$$

In this case the overall problem should be split into two subproblems using linear superposition. The first subproblem will have the expansion

$$u^{(1)}(\rho,\theta)=\sum_{j=0}^{\infty}\rho^{j+\beta}\big(A_j(\theta)\ln\rho+B_j(\theta)\big),$$

with $F^{(1)}(\rho)=F(\rho)$ and $H^{(1)}(\rho)=0$ as the boundary data. Likewise, the second expansion will have the form

$$u^{(2)}(\rho,\theta)=\sum_{j=0}^{\infty}\rho^{j+\gamma}\big(A_j(\theta)\ln\rho+B_j(\theta)\big),$$

with $F^{(2)}(\rho)=0$ and $H^{(2)}(\rho)=H(\rho)$, respectively.

2.2. Curved boundaries

In this section, we build an asymptotic expansion of the solution to the Helmholtz equation (1a):

$$\left(\frac{\partial^2}{\partial x^2}+\frac{\partial^2}{\partial y^2}\right)u(x,y)+k^2u(x,y)=0 \tag{50}$$

near a point on the curved (i.e., non-straight) boundary where the data undergo a discontinuity. We assume that the domain Ω is a disk of radius R centered at the origin on the (x,y)-plane.[5] Introducing the polar coordinates (r,φ), we can write the boundary condition (1b) as follows:

$$u|_{r=R}=\phi_\Gamma(\varphi). \tag{51}$$

The function $\phi_\Gamma(\varphi)$ and/or its derivatives may have jump discontinuities for some given values of φ. Furthermore, the wavenumber k in Eq. (50) may, in general, vary with coordinates, $k=k(x,y)$, and we have chosen a constant wavenumber only for simplicity, since it becomes a variable quantity after the conformal mapping that we introduce below.

Let $\varphi=0$ be one of the points on the boundary where $\phi_\Gamma(\varphi)$ and/or its derivatives is discontinuous.[6] We would like to build an asymptotic expansion to the solution of Eq. (50) in the vicinity of $(R,0)$. For that purpose, we will use a conformal mapping $z=x+iy\mapsto\zeta=\xi+i\eta$ that will help reduce the problem to the case we have analyzed previously, in Section 2.1. Specifically, the fractional linear transform

$$\zeta=i\frac{R-z}{R+z} \tag{52}$$

maps the disk of radius R onto the half-plane $\eta\ge 0$ in the (ξ,η)-coordinates (see Fig. 2). The upper (lower) semi-circle is mapped onto the positive (negative) real semi-axis $\xi>0$ ($\xi<0$). The point $(R,0)$ is mapped into the origin $(0,0)$ of the (ξ,η)-plane whereas the opposite point $(-R,0)$ corresponds to $\pm\infty$ on the real axis ξ.

[5] In Section 1.1, we have indicated that the radius of the circle can be taken as $R=1$ for simplicity; this will be our choice for the numerical simulations of Section 4 as well. Moreover, the choice of a circular shape in the first place is also only a matter of convenience as it makes the conformal mapping that we are going to use particularly simple (fractional linear). Otherwise, it does not present a loss of generality, and our technique can, in fact, address a singularity at the vertex of an arbitrary wedge with curved sides.

[6] This assumption involves no loss of generality as we can always rotate the frame.

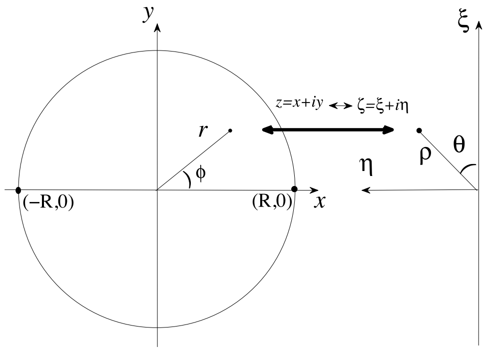

Fig. 2. Conformal mapping (52).

It is well known that under a general conformal mapping $\zeta = \zeta(z)$, the Helmholtz equation (50) transforms as follows:

$$\left(\frac{\partial^2}{\partial \xi^2} + \frac{\partial^2}{\partial \eta^2}\right) u(\xi, \eta) + \left|z'(\zeta)\right|^2 k^2 u(\xi, \eta) = 0, \tag{53}$$

where $z = z(\zeta)$ is the function inverse to $\zeta = \zeta(z)$, and a prime denotes differentiation (in the Cauchy–Riemann sense). For mapping (52), Eq. (53) becomes:

$$\left(\frac{\partial^2}{\partial \xi^2} + \frac{\partial^2}{\partial \eta^2}\right) u(\xi, \eta) + \frac{4k^2 R^2}{[(\xi+1)^2 + \eta^2]^2} u(\xi, \eta) = 0, \tag{54}$$

and we observe that now the wavenumber varies as a function of ξ and η. The boundary condition (51) for Eq. (54) is set on the real axis ξ (i.e., the axis $\eta = 0$):

$$u(\xi, 0) = f(\xi), \tag{55}$$

where the function $f(\cdot)$ is obtained from the original $\phi(\cdot)$ of (51) via the inverse transform $z = z(\zeta)$. Any discontinuities of the boundary data at the point $\varphi = 0$ in (51) are therefore translated to the point $\xi = 0$ after the mapping (52).

Next, we introduce polar coordinates $\xi = \rho\cos\theta$, $\eta = \rho\sin\theta$ on the (ξ, η)-plane, see Fig. 2, and recast equation (54) on the half-plane $\eta \geqslant 0$ in terms of ρ and θ. This yields the Helmholtz equation in the form (36) with the variable wavenumber

$$k^2(\rho, \theta) = \frac{4k^2 R^2}{[1 + \rho^2 + 2\rho\cos\theta]^2}, \tag{56}$$

where the constant k is the physical wavenumber introduced in (50).

Thus, we have reduced the original problem (50–51) formulated on the disk Ω to the Helmholtz equation with variable wavenumber (56) to be solved on the semi-plane $0 \leqslant \theta \leqslant \pi$. In the framework of Section 2.1, this semi-plane can be interpreted as a wedge with the angle $\omega = \pi$, and the location of singularity in the solution of Eq. (36), (56) will be $\rho = 0$. Accordingly, boundary condition (55) on the ξ-axis is reformulated as two conditions on two sides of the wedge:

$$\begin{aligned} u|_{\theta=0} &= f(\rho), \\ u|_{\theta=\pi} &= f(-\rho). \end{aligned} \tag{57}$$

Next, we express the variable wavenumber (56) in the form (39). To do so, we merely expand the right-hand side of (56) in Taylor series with respect to ρ while treating θ as a parameter:

$$k^2(\rho, \theta) = \underbrace{4(kR)^2}_{\equiv k_0(\theta)} + \underbrace{\left(-16(kR)^2 \sin\theta\right)}_{\equiv k_1(\theta)} \rho + \underbrace{8(kR)^2 \left(6\sin^2\theta - 1\right)}_{\equiv k_2(\theta)} \rho^2 + \ldots. \tag{58}$$

Then, we apply the approach of Section 2.1 to the plane wedge with the angle $\omega = \pi$. Then, having obtained the desired number of terms in the asymptotic expansion of the solution in polar coordinates (ρ, θ), we transform them into the original (x, y) or (r, φ) coordinates using the inverse of the conformal mapping (52). The relationship between (ρ, θ) and (x, y) under mapping (52) is

$$\rho(x, y) = \sqrt{\frac{(x-R)^2 + y^2}{(x+R)^2 + y^2}}, \tag{59}$$

$$\theta(x, y) = \begin{cases} \arctan \frac{R^2 - x^2 - y^2}{2Ry}, & y > 0, \\ \pi + \arctan \frac{R^2 - x^2 - y^2}{2Ry}, & y < 0. \end{cases} \tag{60}$$

As we see from (59), $\rho(x, y) \to 0$ as $x \to R$ and $y \to 0$. This is expected since the point $(R, 0)$ is mapped into the origin of the (ξ, η) frame, where $\rho(\xi, \eta) = \sqrt{\xi^2 + \eta^2} \to 0$ as $\xi, \eta \to 0$. On the other hand, when $x \to -R$ and $y \to 0$, $\rho(x, y)$ becomes unbounded since the point $(-R, 0)$ corresponds to $\pm\infty$ on the real axis ξ. Therefore, expansion (40), which is designed to approximate the solution near $(R, 0)$, becomes unbounded at the opposite point $(-R, 0)$ and cannot be used in the vicinity of this point even formally. The latter circumstance is important from the implementation viewpoint (see the discussion in the description of Test 1 in Section 2.3).

Later, we will also need to consider the behavior of several functions of ρ and θ in the vicinity of the point $(R, 0)$. The corresponding analysis is most straightforward in the (ξ, η) coordinates at the origin $(0, 0)$. Since mapping (52) is analytic near this point, the analytical properties of a given function established in the (ξ, η) coordinates will remain the same in the (x, y) or (r, φ) coordinates. Omitting the simple calculations, we present the following results:

- Function (60) is undefined at the point $(R, 0)$ and its first partial derivatives are unbounded there.
- Any combination $\rho^j\theta$, where j is a non-negative integer, has unbounded derivatives at $(R, 0)$ starting from order $(j+1)$.
- Products of the kind $\rho^j \sin j\theta$, $\rho^j \cos j\theta$, $\rho^j \sin((j-2)\theta)$, $\rho^j \cos((j-2)\theta)$ are regular with all of their derivatives at $(R, 0)$.
- The j-th derivative of the term $\rho^j \ln\rho$ is discontinuous at $(R, 0)$.

Finally, we emphasize that a small region near the vertex of any curvilinear wedge can be conformally mapped onto a small region near the vertex of a straight angle. Therefore, the same approach as we are presenting here for the disk will apply to more complicated geometries as well.

2.3. Test problems

In this section, we introduce six test problems with discontinuous boundary conditions set on the circle of radius R. The first three tests correspond to the Dirichlet problem with a jump discontinuity in (i) the boundary data itself, (ii) the first tangential derivative, and (iii) the second tangential derivative. The remaining three tests correspond to the Neumann problem with singularities in the boundary data and their first and second tangential derivatives. We discuss Test 1 in greater detail as an example, leaving the description of the other test problems for Appendix A.

Test 1 We consider piecewise constant Dirichlet data for Eq. (36) with $k^2(\rho, \theta)$ given by (56):

$$u|_{r=R} = \begin{cases} 1, & 0 < \varphi < \pi, \\ 0, & \pi < \varphi < 2\pi. \end{cases} \tag{61}$$

The Dirichlet data (61) undergo a unit jump at $\varphi = 0$ and at $\varphi = \pi$. After the transformation (52), boundary condition (57) for the piecewise constant data (61) reads:

$$\begin{aligned} &u|_{\theta=0} = 1, \\ &u|_{\theta=\pi} = 0. \end{aligned} \tag{62}$$

Next, we solve Eqs. (41–42) consecutively for the first five pairs of coefficients $A_j(\theta)$, $B_j(\theta)$. According to (62), we take $f_0 = 1$, $h_0 = 0$, and $f_j = h_j = 0$ for $j = 1, 2, 3, 4$ in the expansion (38), while k_j are given by (58). The solution we arrive at is the following:

$$\begin{aligned}
&A_0(\theta) = A_1(\theta) = A_3(\theta) \equiv 0, \\
&A_2(\theta) = -\frac{k^2R^2}{\pi}\sin 2\theta, \\
&A_4(\theta) = \frac{k^2R^2}{3\pi}\left[\left(3 - k^2R^2/4\right)\sin 4\theta + k^2R^2\sin 2\theta\right], \\
&B_0(\theta) = 1 - \frac{\theta}{\pi}, \qquad B_1(\theta) = C_1^{(B)}\sin\theta, \\
&B_2(\theta) = C_2^{(B)}\sin 2\theta + k^2R^2\left(1 - \frac{\theta}{\pi}\right)(\cos 2\theta - 1), \\
&B_3(\theta) = C_3^{(B)}\sin 3\theta - C_1^{(B)}\frac{1}{2}k^2R^2\sin\theta + \frac{2k^2R^2}{\pi}\left(\frac{1}{2}\sin 2\theta + 1 - \frac{\theta}{\pi}\right)\sin\theta,
\end{aligned} \tag{63}$$

$$\begin{aligned} B_4(\theta) &= C_4^{(B)} \sin 4\theta - C_2^{(B)} \frac{1}{3} k^2 R^2 \sin 2\theta + C_1^{(B)} \frac{4}{3} k^2 R^2 \sin^4 \theta \\ &\quad - \frac{k^2 R^2}{6\pi} \bigg[(\theta - \pi)(\cos 2\theta - 1)\big((k^2 R^2 - 12) \cos 2\theta - k^2 R^2 \big) \\ &\quad - \frac{1}{24} \sin 2\theta \big(3 \cos 2\theta (k^2 R^2 - 12) - 16 k^2 R^2 - 96 \big) \bigg]. \end{aligned} \tag{64}$$

For convenience, we introduce a shorthand notation for the truncated asymptotic expansion at the point $(R, 0)$ [cf. formula (40)]:

$$u^{(R,0)} = \sum_{j=0}^{4} u_j^{(R,0)}, \tag{65}$$

where

$$u_j^{(R,0)} = \rho^j \big(A_j(\theta) \ln \rho + B_j(\theta) \big). \tag{66}$$

Again, in practice, ρ and θ in formulae (63–66) should be regarded as functions of the coordinates (x, y) or (r, φ) on the disk according, e.g., to transformation (59–60).

Each subsequent term in the sum (65) is more regular than the previous term, i.e., a singularity appears in the derivatives of (at least) one order higher than that for the previous term. Indeed, for each individual term (66) we can write with the help of (63–64) and the considerations on regularity presented (in the form of a bulleted list) at the end of Section 2.2:

$$u_j^{(R,0)} = \ldots \underbrace{\rho^j \ln \rho}_{\substack{j\text{-th derivative} \\ \text{is discontinuous}}} + \ldots \underbrace{\rho^j \theta}_{\substack{(j+1)\text{-th derivatives} \\ \text{are discontinuous}}} + \ldots. \tag{67}$$

In formula (67), the dots substitute for the unimportant multiplicative constants, as well as for the regular terms. We thus see that the lowest order discontinuous derivative is the j-th derivative that appears in the logarithmic term.

At this point, we can justify why we have truncated expansion (40) after $j = 4$, i.e., why we took exactly five terms in expansion (65). According to (67), with five terms used in (65) the difference $v = u - u^{(R,0)} = \sum_{j \geqslant 5} \rho^j (A_j(\theta) \ln \rho + B_j(\theta))$ will be free of the first five low-order terms that may exhibit a singularity at the point $(R, 0)$, and its expansion will start with the terms $\propto \rho^5$, thereby guaranteeing the continuity of all derivatives up to the fourth order.

Moreover, a direct calculation suggests that the terms $u_j^{(R,0)}$ of (66) with the coefficients (63–64) do not satisfy the Helmholtz equation. Therefore the right-hand side of the regularized problem (35) is nonzero in this case (which is also to be expected in general):

$$f = -\boldsymbol{L} u^{(R,0)} = \boldsymbol{L}\big(u - u^{(R,0)} \big) = \boldsymbol{L} v. \tag{68}$$

In (68), we have taken into account that $\boldsymbol{L} u = 0$ for the exact solution u. The degree of regularity of f given by (68) is important from the standpoint of using the compact scheme (3), because the five node stencil applied to f on the right-hand side of (3) renders a central difference approximation of the second derivatives of f, see [8,17,3]. Those derivatives are guaranteed to be continuous if expansion (65) contains at least five terms.

To summarize, we differentiate $v = u - u^{(R,0)}$ four times altogether, with every differentiation reducing the degree of regularity by one. Therefore, to maintain the continuity and boundedness of all quantities employed by our numerical algorithm we need an expansion that is four times continuously differentiable. This is facilitated by taking at least five terms in (65).

The boundary data for the regularized problem (35) are given by $u - u^{(R,0)}|_{r=R}$. For the current test case, the asymptotic solution $u^{(R,0)}$ takes a very simple form on the circle $r = R$. Indeed, the function $\theta(x, y)$ of (60) is equal either to zero (for $y > 0$) or to π (for $y < 0$) at $r = R$. Therefore, according to (63–64), $u^{(R,0)}$ equals one on the upper semi-circle and equals zero on the lower semi-circle. Taking into account the boundary conditions (61), we conclude that the Dirichlet boundary data for the regularized problem are zero on the entire circle $r = R$. In general (see Appendix A), the regularity of the boundary data for the regularized problem matches that of the solution to the regularized problem.

It is also to be noted that the expansion of the truncation error for scheme (3) starts with sixth order derivatives of the solution, see [8,17,3]. To maintain their boundedness, we would formally need to include additional terms into the sum (65) beyond $j = 4$; however, as demonstrated by our numerical experiments in Section 4, taking five terms proves sufficient for restoring the design fourth order convergence rate of the method of difference potentials if applied to the regularized problem (35) or, equivalently, (2a–2b).

Finally, we note that the asymptotic expansion $u^{(-R,0)}$ at the opposite singular point $(-R, 0)$ can be obtained with no additional effort, by an even reflection about the y axis (i.e., $x \mapsto -x$, $y \mapsto y$ in the expressions (59–60)), because the original problem with boundary data (61) possesses this symmetry. This symmetric configuration has been chosen for simplicity; it presents no loss of generality. To suppress the singularities of the solution at both singular points, $(R, 0)$ and $(-R, 0)$, one should use the sum $u^{(R,0)} + u^{(-R,0)}$ of the corresponding asymptotic expansions.

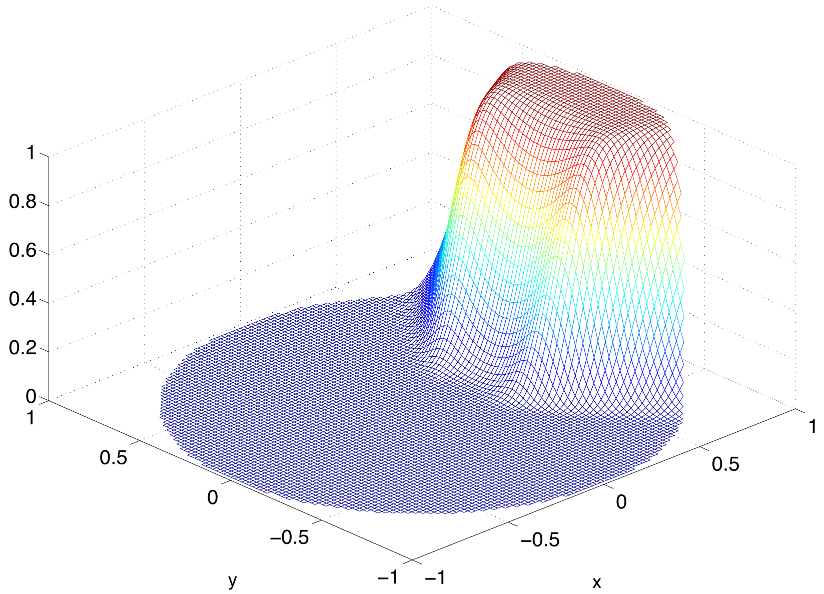

Fig. 3. Function (70) on the disk $R = 1$. The parameters are $r_1 = 0.1$, $r_2 = 0.9$, $\varphi_1 = \pi/12$, $\varphi_2 = \pi/3$.

Implementation notes First of all, the coefficients $B_j(\theta)$ given by (64) include some undetermined constants $C_j^{(B)}$, see Eq. (45) and the discussion that follows. From the standpoint of theory, this uncertainty presents no problem. In practice, however, we must still decide how to handle it.

We again refer to the bulleted list at the end of Section 2.2 and see that all the terms in the expressions $B_j(\theta)\rho^j$, $j = 0, \ldots, 4$, except those that contain θ as a factor are regular at $(R, 0)$ with all their derivatives. We also recall that the sole purpose of using the truncated asymptotic expansion (65) is to subtract it from the exact solution and thereby remove the near-boundary singularity or, more precisely, reduce it to a level beyond which the finite difference scheme becomes insensitive to higher order singular terms. Therefore, keeping the aforementioned regular terms in or dropping them from (65) will make no difference as far as achieving our key goal,[7] which is restoring the design convergence rate of the numerical method. As such, we can set the undetermined coefficients $C_j^{(B)}$ to zero for convenience. Moreover, we could have omitted all other terms in the expressions for $B_j(\theta)$ except those containing θ because those terms are regular as well. However, we have chosen to keep them in our tests since having or not having an additional regular component in the expansion will not affect the numerical performance in any way. Indeed, the only essential requirement of the regularized problem (2a–2b) or (35) is that its solution must be sufficiently smooth so as to re-enable the design high order of accuracy of the scheme. If this requirement is met, then the regularized problem can be solved numerically, and the solution to the original problem can subsequently be restored by adding back the previously subtracted singular part.

Next, to compute the right-hand side for the regularized problem, one applies the Helmholtz operator to the sum of the asymptotic expansions, $u^{(R,0)} + u^{(-R,0)}$. Hence, the latter must be known everywhere on the disk Ω. As, however, has been mentioned, the function $\rho(x, y)$ given by (59) is unbounded at the opposite point $(-R, 0)$, and, consequently, the function $u^{(R,0)}$ is not defined there. Likewise, the function $u^{(-R,0)}$ is not defined at the point $(R, 0)$. Therefore, to achieve the desired regularization, instead of subtracting $(u^{(R,0)} + u^{(-R,0)})$ from the exact solution u, we will first modify $u^{(R,0)}$ and $u^{(-R,0)}$ in a particular way and then subtract:

$$v = u - \left(\mu^{(R,0)}u^{(R,0)} + \mu^{(-R,0)}u^{(-R,0)}\right). \tag{69}$$

The multipliers $\mu^{(R,0)}$ and $\mu^{-R,0)}$ in Eq. (69) are smooth functions equal to unity on some neighborhood of $(R, 0)$ and $(-R, 0)$, receptively. Further away from $(\pm R, 0)$, those multipliers gradually decay to zero. An example of a suitable $\mu^{(R,0)}$ on the unit disk is shown in Fig. 3. The function $\mu^{(-R,0)}$ is an even reflection of $\mu^{(R,0)}$ around the y axis.

What Fig. 3 actually represents is the function defined in polar coordinates:

$$\mu^{(R,0)}(r, \varphi) = \mu_r(r)\mu_\varphi(\varphi), \tag{70}$$

where

$$\mu_r(r) \equiv P_6\left(\frac{r - r_1}{r_2 - r_1}\right), \tag{71}$$

[7] The same applies not only to the genuine regular terms but also to the terms that have sufficiently many continuous derivatives.

$$\mu_\varphi(\varphi) \equiv \begin{cases} 1 - P_6(\frac{\varphi-\varphi_1}{\varphi_2-\varphi_1}), & 0 < \varphi < \pi, \\ 1 - P_6(-\frac{\varphi+\varphi_1}{\varphi_2-\varphi_1}), & -\pi < \varphi < 0, \end{cases} \tag{72}$$

and

$$P_6(x) = \begin{cases} 0, & x < 0, \\ x^7(924x^6 - 6006x^5 + 16380x^4 - 24024x^3 + 20020x^2 - 9009x + 1716), & 0 < x < 1, \\ 1, & x > 1. \end{cases} \tag{73}$$

The univariate function $P_6(x)$ grows smoothly from zero to one on the interval $[0, 1]$. Its first six derivatives are continuous at both endpoints, $x = 0$ and $x = 1$, where they all are equal to zero, while the seventh derivative undergoes a jump. In (71), r_1 and r_2 denote some positive numbers such that $r_1 < r_2 < R$. Therefore, the function $\mu_r(r)$ of (71) smoothly increases from zero to one in the radial direction on the annulus $\{r_1 \leqslant r \leqslant r_2\}$, i.e., strictly inside the disk $\Omega = \{0 \leqslant r \leqslant R\}$. Similarly, the angles φ_1 and φ_2 are chosen so that $0 < \varphi_1 < \varphi_2 < \pi$. Then, the function $\mu_\varphi(\varphi)$ of (72) is equal to one in the sector $|\varphi| \leqslant \varphi_1$, symmetrically decays to zero for $\varphi_1 < |\varphi| < \varphi_2$, and vanishes for $|\varphi| \geqslant \varphi_2$. Altogether, this guarantees the desired behavior of $\mu^{(R,0)}$ of (70).

We emphasize that the multiplies $\mu^{(\pm R,0)}$ introduced in (69) are, of course, going to affect both the right-hand side, see formula (68), and the boundary data of the regularized problem (35). The resulting final formulation of the regularized problem that is actually solved numerically by the method of difference potentials is presented in Section 3.1.

The remaining five test cases are described in detail in Appendix A. Out of the five, two are Dirichlet problems with near-boundary singularities of decreasing strength — one is due to a jump discontinuity in the first derivative of the data function and the other is due to a jump discontinuity in the second derivative of the data function. The rest are Neumann problems, altogether three, and they also have near-boundary singularities of decreasing strength, due to a jump in the data function itself, its first derivative, and its second derivative, respectively. In Appendix A, we present the boundary conditions for the remaining five test problems (that replace (61)) and provide the coefficients of their asymptotic expansions. In this section, we make a few general comments:

- For all the tests, we use symmetry w.r.t. the y axis to obtain the expansion $u^{(-R,0)}$.
- The undetermined coefficients $C_j^{(B)}$ are set to zero in all tests.
- The multipliers $\mu^{(\pm R,0)}$, see (70), are used in all the tests to enable the independent treatment of each individual singular point.
- The degree of smoothness and the number of terms in the expansion are determined as follows. In the Dirichlet tests with the discontinuous first and second derivatives the non-trivial (i.e., non-constant) terms in the asymptotic expansion begin with the functions $u_1^{(\pm R,0)}$ and $u_2^{(\pm R,0)}$, respectively. Hence, the solution in these cases is smoother than that of Test 1, which is natural because the boundary data are smoother. Nevertheless, even for these smoother settings we should truncate the expansion exactly at the same level (at $u_4^{(\pm R,0)}$ term) as for Test 1 to maintain the desired smoothness of the right-hand side.
- The asymptotic expansion for the Neumann problems takes the form (49), with the respective exponents greater by one than those in the Dirichlet expansion (40). Therefore, we can truncate the Neumann expansion at one term earlier (at $j = 3$), which proves sufficient for the regularized difference v to have four continuous derivatives.

3. Solution by difference potentials in the presence of singularities

3.1. Regularized problem

Assume now that we have a boundary value problem (1a), (1b) on the unit disk Ω with boundary condition (1b) that is not smooth at the points $\varphi = 0$ and $\varphi = \pi$ on the unit circle Γ. We then build the appropriate singular functions $\{u_j^{(R,0)}\}_{0=1}^M$ via the methods of Section 2 (for all the examples of Section 2.3 and Appendix A, it proves sufficient to take $M = 4$) and formulate the regularized BVP (2a–2b) by subtracting the singular functions multiplied by the cutting function $\mu^{(R,0)}$ from the solution u in the original BVP (1a–1b). By taking advantage of symmetry that helps us address the opposite singular point $(-R, 0)$ with no additional effort and collecting the known terms on the right-hand side, we arrive the regularized BVP, for which we have previously used the generic notation (2a–2b) [cf. Eqs. (35), (68), and (69)]:

$$\boldsymbol{L}u = -\sum_{j=0}^{M} \boldsymbol{L}\big(\mu^{(R,0)} u_j^{(R,0)}\big) - \sum_{j=0}^{M} \boldsymbol{L}\big(\mu^{(-R,0)} u_j^{(-R,0)}\big) \stackrel{\text{def}}{=} f, \quad x \in \Omega, \tag{74a}$$

$$\boldsymbol{l}_\Gamma u = \phi_\Gamma - \sum_{j=0}^{M} \boldsymbol{l}_\Gamma\big(\mu^{(R,0)} u_j^{(R,0)}\big) - \sum_{j=0}^{M} \boldsymbol{l}_\Gamma\big(\mu^{(-R,0)} u_j^{(-R,0)}\big) \stackrel{\text{def}}{=} \psi_\Gamma. \tag{74b}$$

In formula (74b), we allow the boundary operator $\boldsymbol{l}_\Gamma$ to specify a Dirichlet or Neumann condition. By design, both the right-and side f of the regularized BVP (74a) and the regularized boundary data ψ_Γ of (74b) are sufficiently smooth on their respective domains, with at least two and four continuous derivatives, respectively, at the singular points $\varphi = 0$ and $\varphi = \pi$ on the boundary Γ.

The method of difference potentials, as described in Sections 1.1–1.5, can now be applied to the regularized problem (74a–74b) without degradation of the design fourth order convergence rate of the overall scheme. Let u_R denote the "regular" solution, i.e., the solution to the regularized problem (74a–74b) by the method of difference potentials, which, for a particular grid $\mathbb{N}$ on the square auxiliary domain, has its values defined on the nodes $\mathbb{N}^+$ (recall that this is the set of interior nodes of Ω plus a "fringe", see Fig. 1). Then the numerical solution u to the original singular problem (1a–1b) at the nodes $\mathbb{N}^+$ is given by simply adding back the singular expressions calculated at these nodes:

$$u|_{\mathbb{N}^+} = u_R + \mu^{(R,0)}\big|_{\mathbb{N}^+} \sum_{j=0}^{M} u_j^{(R,0)}\Bigg|_{\mathbb{N}^+} + \mu^{(-R,0)}\big|_{\mathbb{N}^+} \sum_{j=0}^{M} u_j^{(-R,0)}\Bigg|_{\mathbb{N}^+}. \tag{75}$$

Therefore, the algorithm for the method of difference potentials presented in Sections 1.1–1.5 does not change at all; in fact, what changes is the problem which we solve by difference potentials. In other words, we rephrase the original singular problem (1a–1b) as the regularized problem (2a–2b) which takes the specific form (74a–74b), apply the method of difference potentials to the regularized problem (74a–74b), and then add back the singular terms as in (75).

3.2. Solution of multiple problems at low cost

The algorithm of the method of difference potentials described in Sections 1.1–1.5 admits computationally inexpensive solutions to problems which share certain similar features. The most expensive component of the algorithm is the application of the projection operator, which involves the inverse $\boldsymbol{G}^{(h)}$ of the finite difference operator $\boldsymbol{L}^{(h)}$, i.e., the solution of the discrete AP (5a–5d), see Section 1.3. Building the matrix $\boldsymbol{Q}_H$ of (25) or (34) that enters into the BEP (26) requires that the projection operator be applied to each basis function once it has been extended to the discrete boundary γ. In the case $\Gamma = \Gamma_1 \cup \Gamma_2$, which corresponds to (34), this amounts to a total of $4(N+1)$ applications of the projection [cf. the number of Chebyshev basis functions in (33)]. Additionally, there will be two applications of the inverse operator $\boldsymbol{G}^{(h)}$ which are associated with the right-hand side f of (74a), one for the term $\boldsymbol{TrG}^{(h)} f$, and one more to compute the inhomogeneous contribution to the extension, $\boldsymbol{Q}_I$. One more application of the projection is required to obtain the final numerical solution since it is expressed by the generalized Green's formula (9) once the system for the Chebyshev coefficients has been solved via *QR*.

Therefore, provided that matrix $\boldsymbol{Q}_H$ is unchanged, the overall computational cost of solving a new problem is small. In particular, this means that we are able to solve problems with different right-hand sides f in (2a) or boundary conditions (2b) without the need to redo the expensive computations associated with applying the projection to each individual basis function. In the numerical simulations of Section 4, all of the problems have singularities at the same locations, $\varphi = 0, \pi$, on the unit circle Γ. Hence, they differ only by the right-hand side of the regularized equation (74a) and the boundary data ψ_Γ in (74b), which result from the singular functions specific to a given problem, see Section 2.3 and Appendix A. Moreover, the change of the type of the boundary condition from Dirichlet to Neumann does not incur any further computational cost either. Consequently, we can solve all those problems by computing $\boldsymbol{Q}_H$ only once and then performing a small amount of additional computations per individual problem at a low cost.

4. Numerical simulations

As indicated in Section 1.1, we will be solving the homogeneous Helmholtz equation (1a) subject to boundary condition (1b) on a disc Ω of radius 1, centered at the origin. For the purpose of using the method of difference potentials, Ω is embedded in an auxiliary domain that is a square of side length 2.2, also centered at the origin, see Section 1.3. We form series expansions of the boundary data using Chebyshev basis functions as described in Section 1.5. The originally posed problem is modified using the method of singularity subtraction outlined in Section 2, with particular singular functions for each problem derived in Section 2.3 and Appendix A. This results in an inhomogeneous problem (2a–2b) or (74a–74b) which no longer has discontinuity in the boundary condition and whose right-hand side is sufficiently smooth. The solution of problem (74a–74b) is therefore expected to possess sufficient regularity so that the method of difference potentials will yield the numerical solution at the design rate of grid convergence for the scheme (3), which is fourth order. After computing the numerical solution to this regularized problem, we add back the singular functions to the numerical solution in order to obtain an approximation to solution of the original singular problem (1a–1b).

4.1. Parameters of the computational setting

In all of the following test problems, the calculations are conducted via the fourth-order accurate compact finite difference scheme (5a) supplemented by the Sommerfeld-type boundary conditions (5c–5d) at the left and right edges of the auxiliary square and a Dirichlet condition (5b) at its top and bottom edges. These computations are carried out on a series of Cartesian grids containing 64, 128, 256, 512, 1024, and 2048 cells uniformly spaced in each direction, with each grid being nested within the previous. We do not suppose, in general, that the exact solution to each problem is known, and thus we use this nesting of the grids to compute the error in the "Cauchy sense," the maximum absolute value of the difference between the two numerical solutions on a pair of consecutive grids, with this difference evaluated at the nodes of the coarser grid. The convention which we adopt in Tables 2–7 is that the coarser grid involved in the computation of the error is shown, and the convergence rates shown are computed as the binary logarithm of the ratios of successive errors. For the first test, we have also found the exact solution explicitly (Section 4.2), which enables a direct study of the grid convergence as an additional validation of our method.

The number of basis functions N used to expand the boundary data according to formula (33) is chosen specifically for each grid and each problem. On one hand, the number of basis functions must approximate the boundary data with accuracy that matches or exceeds the accuracy of the finite difference scheme (5a–5d). On the other hand, having too many basis functions on a given grid will result in a loss of accuracy. The reason is that each Chebyshev basis function is more oscillatory than the previous one. Eventually, for a particular grid, a basis function is reached whose oscillations are finer than the grid size, and hence all subsequent basis functions become essentially indistinguishable by the grid. This artificial loss of accuracy is alleviated when moving to finer grids, which may give the false impression of an unusually high convergence rate. We have observed by trial-and-error that the threshold for the loss of accuracy due to having too many basis functions on the coarsest grid, 64×64, is around $N = 45$ basis functions. Therefore, we adhere to the following strategy of determining the appropriate number of basis functions in each case:

1. We run the simulation first on the coarsest grids, 64×64 and 128×128, using 45 basis functions on each. By saving the matrix $\boldsymbol{Q}_H$ from each test, we can very cheaply reduce the number of basis functions in subsequent simulations by simply eliminating the corresponding columns of $\boldsymbol{Q}_H$, or, if we instead wish to add more basis functions, we may also prevent redundant computation by only computing the additional columns of $\boldsymbol{Q}_H$ that we desire.
2. We run the simulation again on the 64×64 grid with fewer and fewer basis functions, computing the error for each test by comparing the solution to the one on the 128×128 grid. At first the error drops because the number of basis functions decreases from $N = 45$, which is too many, to smaller values. Then, it reaches what we will refer to as the "grid error" — that is, the error which is free from both the interference due to oscillations in higher basis functions and from the insufficiently accurate approximation of the boundary data. The design rate of grid convergence can be observed if the number of basis functions falls into this middle range (not too many, but enough for approximating the boundary data), which is different for each grid.
3. Once the grid error has been determined, we compute the truncation error of the Chebyshev expansion of the boundary data for the minimum number of basis functions which yields the grid error. This truncation error can be evaluated by computing the expansion with many more basis functions and then looking at the maximum absolute value of the coefficients beyond the chosen point which yields the grid error.
4. Now, knowing that the finite difference scheme is fourth order accurate, and that our consecutive grids will each have twice as many nodes in each direction, we expect that the grid error for the 128×128 grid will be smaller than that of the 64×64 grid by a factor of 16. Therefore, we obtain the necessary truncation error for the Chebyshev series on the 128×128 grid by dividing the truncation error of the Chebyshev series obtained on the 64×64 grid by 16, and then determine the number of coefficients required to achieve this truncation error on the finer grid. The resulting number of coefficients should be sufficient to achieve the grid error on the 128×128 grid. According to step 1, we may need to compute only the additional columns of $\boldsymbol{Q}_H$ that correspond to the basis functions beyond $N = 45$, if necessary.
5. For all subsequent grids, we continue to divide the truncation error obtained in step 4 by another factor of 16 (so that for the grid 256×256, we are dividing the original truncation error by 16^2, and so on) and then find the appropriate number of Chebyshev terms corresponding to that grid the same way as before.

Note that if the Chebyshev expansions of the boundary functions converge too slowly, then the minimum number of basis functions required to represent the boundary data may exceed the capability of the grid to resolve the basis functions. However, this has never been observed in practice and is, in fact, prevented by design. Recall that the convergence of the Chebyshev series depends on the smoothness of the function being expanded, see the comments right after Eq. (29). While the original boundary data in our problems are discontinuous, the boundary data are "smoothened" by the process of singularity subtraction, so that the data on which we perform the expansion have at least 4 continuous derivatives. This has proven to be sufficient for our case, as the results in Tables 2–7 confirm. Since the number of basis function on each grid depends on the boundary data of the problem, our particular choices are displayed in Tables 2–7.

The circular boundary Γ is partitioned into two arcs which meet, by design, at the discontinuity locations of the boundary data, so that $\Gamma_1 = \{r = 1,\ 0 < \varphi < \pi\}$, $\Gamma_2 = \{r = 1,\ \pi < \varphi < 2\pi\}$. Thus, the trace of the solution along each arc of the circle is independently represented by its own set of Chebyshev basis functions.[8] We implement the Chebyshev basis functions on an extended interval $[-1 - \varepsilon, 1 + \varepsilon]$ in order to avoid numerical difficulties that arise when computing the

[8] These bases need not have the same dimensions: neither the bases on each arc or even the bases for the Dirichlet or Neumann portions of the data need to match. That is, we could instead assign altogether 4 different numbers of basis functions, one for each of the two arcs and one for each component of the Cauchy data on each arc. It is only for convenience that we use the same number of basis functions N on each arc and each component of the data.

Table 1
Results for Dirichlet boundary data with discontinuity.

Grid	$k=5$			$k=15$		
	N	Error	Conv. rate	N	Error	Conv. rate
64×64	30	2.46	–	40	0.73	–
128×128	30	6.40×10^{-4}	11.91	40	4.72×10^{-2}	3.96
256×256	45	2.48×10^{-5}	4.69	50	3.02×10^{-3}	3.97
512×512	70	1.58×10^{-6}	3.97	53	1.91×10^{-4}	3.99
1024×1024	81	3.60×10^{-7}	2.13	71	1.19×10^{-5}	4.00

Table 2
Results for Dirichlet boundary data with discontinuity. The error is computed by comparison to the approximation (77) of the exact solution.

Grid	$k=5$			$k=15$		
	N	Error	Conv. rate	N	Error	Conv. rate
64×64	30	2.4×10^{-3}	–	40	0.81	–
128×128	30	1.39×10^{-4}	4.11	40	5.58×10^{-2}	3.86
256×256	45	2.33×10^{-6}	5.90	50	3.21×10^{-3}	4.12
512×512	70	1.15×10^{-7}	4.34	53	2.03×10^{-4}	3.99
1024×1024	81	8.38×10^{-9}	3.78	71	1.27×10^{-5}	3.99

derivatives of the Chebyshev functions near the endpoints of the interval $[-1, 1]$. In all of the simulations, this parameter is chosen to be $\varepsilon = 0.001$ (for details on the choice of this parameter, see [4]).

The computer implementation of the algorithm is performed in MATLAB.

4.2. Test 1: discontinuous Dirichlet boundary data

The specified Dirichlet condition is discontinuous,

$$u|_{r=1} = \begin{cases} 1, & 0 < \varphi < \pi, \\ 0, & \pi < \varphi < 2\pi, \end{cases}$$

and the coefficients of the singular terms are given by (63–64). The results are presented in Table 1.

As an additional corroboration of the performance of the method, in Table 2 we present a comparison to the exact solution for this test problem:

$$u(r,\varphi) = \frac{1}{2}\frac{J_0(kr)}{J_0(kR)} + \frac{2}{\pi}\sum_{n=0}^{\infty}\frac{J_{2n+1}(kr)}{J_{2n+1}(kR)}\frac{\sin(2n+1)\varphi}{2n+1}, \tag{76}$$

where J_n are the Bessel functions of the first kind and R is the radius of the circle, which in our case is $R = 1$. In practice, we must make a few modifications in order to evaluate (76) with sufficient accuracy. First, we truncate the series expansion at 2000 terms. Next, for terms of the series beyond the 50-th we replace the ratio of Bessel functions by its asymptotic form r^{2n+1} due to a loss of numerical stability in computing higher order Bessel functions. Therefore, we approximate the solution as follows:

$$u(r,\varphi) = \frac{1}{2}\frac{J_0(kr)}{J_0(kR)} + \frac{2}{\pi}\left[\sum_{n=0}^{50}\frac{J_{2n+1}(kr)}{J_{2n+1}(kR)}\frac{\sin(2n+1)\varphi}{2n+1} + \sum_{n=51}^{2000} r^{2n+1}\frac{\sin(2n+1)\varphi}{2n+1}\right]. \tag{77}$$

One final note is that the series (76) converges poorly near the boundary of the disk, $R = 1$. To overcome this, we compare the numerical solution to the expansion (77) only on the interior 90% of the disk (i.e., on the subset $r < 0.9$).

4.3. Test 2: continuous Dirichlet boundary data with first derivative discontinuity

For this problem, the Dirichlet condition is discontinuous in the first derivative,

$$u(\varphi) = \begin{cases} \frac{\pi}{2} - \varphi, & 0 < \varphi < \pi, \\ \varphi - \frac{3\pi}{2}, & \pi < \varphi < 2\pi, \end{cases}$$

and the coefficients of the singular terms are given by (80–81). The results are shown in Table 3.

Table 3
Results for continuous Dirichlet boundary data with first derivative discontinuity.

Grid	$k = 1$			$k = 5$		
	N	Error	Conv. rate	N	Error	Conv. rate
64 × 64	40	0.39	–	40	0.80	–
128 × 128	50	7.42×10^{-5}	12.36	40	1.83×10^{-4}	12.09
256 × 256	66	5.60×10^{-6}	3.73	50	7.18×10^{-6}	4.67
512 × 512	82	3.16×10^{-7}	4.15	74	4.42×10^{-7}	4.02
1024 × 1024	111	2.10×10^{-8}	3.91	111	2.63×10^{-8}	4.07

Table 4
Results for continuous Dirichlet boundary data with second derivative discontinuity.

Grid	$k = 1$			$k = 5$		
	N	Error	Conv. rate	N	Error	Conv. rate
64 × 64	40	0.97	–	40	7.55	–
128 × 128	50	4.34×10^{-4}	11.12	40	1.19×10^{-4}	15.95
256 × 256	66	3.82×10^{-5}	3.50	56	1.48×10^{-5}	3.01
512 × 512	76	2.33×10^{-6}	4.03	86	7.77×10^{-7}	4.25
1024 × 1024	110	1.41×10^{-7}	4.05	124	4.76×10^{-8}	4.03

Table 5
Results for Neumann boundary data with discontinuity.

Grid	$k = 1$			$k = 5$		
	N	Error	Conv. rate	N	Error	Conv. rate
64 × 64	40	0.26	–	40	3.57	–
128 × 128	50	7.60×10^{-5}	11.71	50	1.30×10^{-4}	14.73
256 × 256	71	6.03×10^{-6}	3.65	57	1.51×10^{-5}	3.11
512 × 512	96	2.62×10^{-7}	4.52	90	8.67×10^{-7}	4.12
1024 × 1024	124	1.47×10^{-8}	4.15	119	7.11×10^{-8}	3.61

4.4. Test 3: continuous Dirichlet boundary conditions with second derivative discontinuity

The Dirichlet boundary condition is now discontinuous in the second derivative,

$$u(\varphi) = \begin{cases} \cos\varphi, & 0 < \varphi < \pi, \\ \cos 3\varphi, & \pi < \varphi < 2\pi, \end{cases}$$

with the coefficients of the singular terms given by (84–85). The results are given in Table 4.

4.5. Test 4: discontinuous Neumann boundary data

The discontinuous Neumann boundary condition for this test is

$$\frac{\partial u}{\partial n}(\varphi) = \begin{cases} 1, & 0 < \varphi < \pi, \\ 0, & \pi < \varphi < 2\pi, \end{cases}$$

and the coefficients of the singular terms are given by (88–89). The results are summarized in Table 5.

4.6. Test 5: continuous Neumann boundary data with first derivative discontinuity

In this test, the Neumann boundary data are discontinuous in the first derivative,

$$\frac{\partial u}{\partial n}(\varphi) = \begin{cases} \frac{\pi}{2} - \varphi, & 0 < \varphi < \pi, \\ \varphi - \frac{3\pi}{2}, & \pi < \varphi < 2\pi, \end{cases}$$

and the coefficients of the singular terms are given by (90–91). The results are shown in Table 6.

4.7. Test 6: continuous Neumann boundary data with second derivative discontinuity

For the final test, the Neumann data have a jump in the second derivative,

$$\frac{\partial u}{\partial n}(\varphi) = \begin{cases} \cos\varphi, & 0 < \varphi < \pi, \\ \cos 3\varphi, & \pi < \varphi < 2\pi, \end{cases}$$

and the coefficients of the singular terms are shown in (92–93). The results are given in Table 7.

Table 6
Results for continuous Neumann boundary data with first derivative discontinuity.

Grid	$k=1$			$k=5$		
	N	Error	Conv. rate	N	Error	Conv. rate
64×64	40	0.55	–	40	0.52	–
128×128	50	1.78×10^{-5}	14.92	50	6.57×10^{-4}	9.64
256×256	76	1.85×10^{-6}	3.26	71	1.35×10^{-5}	5.61
512×512	94	1.90×10^{-7}	3.28	96	2.90×10^{-7}	4.78
1024×1024	128	8.97×10^{-9}	4.40	122	2.66×10^{-8}	4.20

Table 7
Results for continuous Neumann boundary data with second derivative discontinuity.

Grid	$k=1$			$k=5$		
	N	Error	Conv. rate	N	Error	Conv. rate
64×64	40	0.83	–	40	5.10	–
128×128	40	5.76×10^{-4}	10.49	40	6.03×10^{-4}	13.05
256×256	60	3.23×10^{-5}	4.15	60	3.47×10^{-5}	4.12
512×512	96	2.32×10^{-6}	3.80	96	1.65×10^{-6}	4.39
1024×1024	126	1.37×10^{-7}	4.08	128	6.62×10^{-8}	4.64

5. Discussion and future work

We have shown how to apply the method of difference potentials when computing singular solutions of the Helmholtz equation while preserving high order accuracy. The key idea is to regularize the original problem by subtracting several leading terms of the asymptotic expansion of the solution near the singularity, and approximate numerically only the remaining sufficiently smooth part of the solution. Then, the finite difference scheme can maintain its consistency, and, as the computations in Section 4 demonstrate, the overall numerical method converges with the design rate. In doing so, the method of difference potentials has also permitted us to handle non-conforming curvilinear boundaries on regular structured grids with no deterioration of accuracy and enables the solution of a series of problems with various boundary conditions at a low computational cost per problem (Section 3.2).

A logical next step would be to consider near-boundary singularities that are due not only to the discontinuities in the data, but also to geometric irregularities, such as (re-entrant) corners or cusps. All of the necessary analysis for this formulation has already been performed in this paper (Section 2). To make the overall approach more general, one will also need to account for other boundary conditions, beyond the Dirichlet and Neumann. An even more comprehensive extension would involve the analysis of singularities at the interface between two materials when solving transmission/scattering problems, see [14], wherein singularities may arise from discontinuities in the interface conditions/data and/or the geometric irregularities of the interface itself.

We also note that neither in this paper, which specifically focuses on singularities, nor in our previous papers devoted to solving the Helmholtz equation by the method of difference potentials, see [4,13,14], we did not analyze the performance of the method in the case of large wavenumbers k. This issue may require additional attention in the future. In the meantime, we only mention that similarly to any other finite difference approach, our methodology is prone to the pollution effect, which is precisely the reason why we use high order accurate schemes, see Section 1.2. Moreover, large wavenumbers may require higher dimensions N of the basis chosen on the boundary Γ, see formula (20). We expect, however, that N will increase slowly, because the solutions we are computing are sufficiently smooth (singularities are removed prior to numerical approximation).

Appendix A. Test problems 2 through 6

Test 2 The Dirichlet boundary data for this test have discontinuous first derivative at $(\pm R, 0)$:

$$u|_{r=R} = \begin{cases} \pi/2-\varphi, & 0<\varphi<\pi, \\ \varphi-3\pi 2, & \pi<\varphi<2\pi, \end{cases}$$

or, after the mapping (52),

$$u(\xi,0) = \begin{cases} \frac{\pi}{2}+\arctan\frac{2\xi}{\xi^2-1}, & \xi>0, \\ \frac{\pi}{2}-\arctan\frac{2\xi}{\xi^2-1}, & \xi<0. \end{cases}$$

Equivalently, in polar coordinates (ρ,θ) on the (ξ,η) plane on the edges of the wedge with angle π we have:

$$u|_{\theta=0} = \frac{\pi}{2} + \arctan\frac{2\rho}{\rho^2-1},$$
$$u|_{\theta=\pi} = \frac{\pi}{2} + \arctan\frac{2\rho}{\rho^2-1}. \tag{78}$$

The Taylor expansion of the data (78) at $\rho = 0$ (which corresponds to the singular point $(R, 0)$) reads:

$$u|_{\theta=0,\pi} = \frac{\pi}{2} - 2\rho + \frac{2}{3}\rho^3 - \frac{2}{5}\rho^5 + \dots \tag{79}$$

Note that the formally identical expressions (78), (79) for the boundary conditions in the coordinates (ρ, θ) undergo a jump in the derivative since the differentiation w.r.t. ρ is done in the opposite directions on the rays $\theta = 0$ and $\theta = \pi$. Moreover, after the conformal mapping the singularity of the boundary data appears in all odd derivatives.

The coefficients of the asymptotic expansion at the point $(R, 0)$ are given by

$$A_0(\theta) = A_2(\theta) = 0, \qquad A_1(\theta) = \frac{4\sin\theta}{\pi},$$
$$A_3(\theta) = \frac{6k^2R^2-4}{3\pi}\sin 3\theta - \frac{2k^2R^2}{\pi}\sin\theta, \qquad A_4(\theta) = \frac{4k^2R^2(\cos 2\theta - 1)^2}{3\pi}, \tag{80}$$

and

$$B_0(\theta) = \frac{\pi}{2}, \qquad B_1(\theta) = C_1^{(B)}\sin\theta + \frac{2(2\theta-\pi)\cos\theta}{\pi},$$
$$B_2(\theta) = C_2^{(B)}\sin 2\theta + \frac{\pi k^2R^2}{2}(\cos 2\theta - 1),$$
$$B_3(\theta) = -\frac{1}{2}k^2R^2\sin\theta C_1^{(B)} + \sin 3\theta C_3^{(B)} + \frac{1}{9\pi}\big[12\big\{\big(6k^2R^2-4\big)\cos^2\theta - 6k^2R^2 + 3\big\}(\theta - \pi/2)\cos\theta$$
$$+ \sin\theta\big\{9k^2R^2\big(\pi^2 + 4/3\big) - 2\big\} + \sin\theta\cos^2\theta\big(8 - 12k^2R^2\big)\big],$$
$$B_4(\theta) = \frac{1}{3}k^2R^2(\cos 2\theta - 1)^2C_1^{(B)} - \frac{1}{3}k^2R^2\sin 2\theta C_2^{(B)} + \sin 4\theta C_4^{(B)}$$
$$- \frac{k^2R^2}{6\pi}\big[\cos^2 2\theta + \big\{8\theta\sin 2\theta - 16/3 + \big(k^2R^2 - 6\big)\pi^2\big\}\cos 2\theta$$
$$+ \big\{\pi^2\big(3 - k^2R^2/4\big) - 7/6\big\}\cos 4\theta + (8\pi - 16\theta)\sin 2\theta + 11/2 + 3\pi^2\big(1 - k^2R^2/4\big)\big]. \tag{81}$$

The asymptotic expansion at the opposite singular point $(-R, 0)$ is obtained from that at the point $(R, 0)$ by an odd reflection about the y axis using the symmetry of the boundary condition.

Test 3 The Dirichlet boundary data for this test have discontinuous second derivative (as well as higher order even derivatives) at the points $(\pm R, 0)$:

$$u|_{r=R} = \begin{cases} \cos\varphi, & 0 < \varphi < \pi, \\ \cos 3\varphi, & \pi < \varphi < 2\pi. \end{cases}$$

After the conformal mapping we have:

$$u(\xi, 0) = \begin{cases} \cos(\arctan\frac{2\xi}{\xi^2-1}), & \xi > 0, \\ \cos(3\arctan\frac{2\xi}{\xi^2-1}), & \xi < 0. \end{cases} \tag{82}$$

Finally, in terms of (ρ, θ) the boundary condition (82) translates into:

$$u|_{\theta=0} = \cos\left(\arctan\frac{2\rho}{\rho^2-1}\right) \underset{\rho\to 0}{\approx} 1 - 2\rho^2 + 2\rho^4 - 2\rho^6 + \dots,$$
$$u|_{\theta=\pi} = \cos\left(3\arctan\frac{2\rho}{\rho^2-1}\right) \underset{\rho\to 0}{\approx} 1 - 18\rho^2 + 66\rho^4 - 146\rho^6 + \dots \tag{83}$$

The coefficients of the asymptotic expansion at the point $(R, 0)$ are:

$$\begin{aligned}
&A_0(\theta) = A_1(\theta) = A_3(\theta) \equiv 0, \qquad A_2 = -\frac{16}{\pi}\sin 2\theta, \\
&A_4(\theta) = \frac{16}{3\pi}\left[\left(12 - k^2R^2\right)\sin 4\theta + k^2R^2\sin 2\theta\right], \\
&B_0(\theta) = 1, \qquad B_1(\theta) = 0, \\
&B_2(\theta) = C_2^{(B)}\sin 2\theta + \left(k^2R^2 - 2 - \frac{16}{\pi}\theta\right)\cos 2\theta + \frac{8}{\pi}\sin 2\theta - k^2R^2, \\
&B_3(\theta) = \sin 3\theta C_3^{(B)} + 2k^2R^2\sin\theta, \\
&B_4(\theta) = -\frac{1}{3}k^2R^2\sin 2\theta C_2^{(B)} + \sin 4\theta C_4^{(B)} + \left(\frac{k^4R^4}{12} - \frac{5k^2R^2}{3} + 2\right)\cos 4\theta \\
&\qquad + \frac{1}{36\pi}\Big[\left(4608 - 384k^2R^2\right)\theta\cos^2 2\theta + \big\{\left(48k^2R^2 - 576\right)\sin 2\theta \\
&\qquad - 12k^2R^2\left(\pi k^2R^2 - 8\pi - 16\theta\right)\big\}\cos 2\theta - 160k^2R^2\sin 2\theta + 9\pi k^4R^4 \\
&\qquad + 192k^2R^2(\theta - 3\pi/16) - 2304\theta\Big].
\end{aligned} \tag{84, 85}$$

Similarly to Test 2, the boundary data are anti-symmetric w.r.t. the y axis, and thus the asymptotic expansion at $(-R, 0)$ is given by an odd reflection of its counterpart at the point $(R, 0)$.

Test 4 This is a Neumann test problem, for which the boundary conditions are set for the normal derivative of the solution. We start with the case of a discontinuity in the normal derivative itself:

$$\left.\frac{\partial u}{\partial r}\right|_{r=R} = \begin{cases} 1, & 0 < \varphi < \pi, \\ 0, & \pi < \varphi < 2\pi. \end{cases}$$

Obviously, the normal derivative undergoes a unit jump in the circumferential direction at the points $(\pm R, 0)$ (cf. formula (61)). It can be easily verified that under the mapping (52) the normal derivative at the boundary in the (ξ, η) coordinates takes the form:

$$\left.\frac{\partial u}{\partial r}\right|_{r=R} = -\frac{1}{2R}\left(1 + \xi^2\right)\left.\frac{\partial u}{\partial \eta}\right|_{\eta=0},$$

where

$$\left.\frac{\partial u}{\partial \eta}\right|_{\eta=0} = \begin{cases} -\frac{2R}{1+\xi^2}, & \xi > 0, \\ 0, & \xi < 0, \end{cases}$$

and the corresponding (ρ, θ) expressions are

$$\begin{aligned}
&\left.\frac{1}{\rho}\frac{\partial u}{\partial \theta}\right|_{\theta=0} = -\frac{2R}{1+\rho^2}, \\
&\left.\frac{1}{\rho}\frac{\partial u}{\partial \theta}\right|_{\theta=\pi} = 0.
\end{aligned} \tag{86}$$

Note that in general the following relation holds between the derivatives:

$$\left.\frac{\partial u}{\partial \eta}\right|_{\eta=0} = -\left.\frac{1}{\rho}\frac{\partial u}{\partial \theta}\right|_{\theta=\pi}, \quad \xi < 0. \tag{87}$$

Hence, one must remember the additional minus sign on the negative semi-axis $\xi < 0$. For this particular test problem though, this issue is obscured by the zero condition on $\xi < 0$.

Finally, the power series expansion of the conditions (86) on the rays $\theta = 0$, $\theta = \pi$ is

$$\begin{aligned}
&\left.\frac{\partial u}{\partial \theta}\right|_{\theta=0} = -\frac{2R\rho}{1+\rho^2} \underset{\rho\to 0}{\approx} -2R\left(\rho - \rho^3 + \rho^5 - \ldots\right), \\
&\left.\frac{\partial u}{\partial \theta}\right|_{\theta=\pi} = 0.
\end{aligned}$$

The coefficients of expansion (49) at the point $(R, 0)$ are given by

$$
\begin{aligned}
&A_0(\theta) = -\frac{2R\cos\theta}{R}, \qquad A_1(\theta) = 0,\\
&A_2(\theta) = \frac{R(2-k^2R^2)}{3\pi}\cos 3\theta + \frac{k^2R^3}{\pi}\cos\theta, \qquad A_3(\theta) = \frac{2k^2R^3}{3\pi}(\sin 4\theta - 2\sin 2\theta),
\end{aligned} \tag{88}
$$

$$
\begin{aligned}
&B_0(\theta) = C_0^{(B)}\cos\theta + \frac{2R}{\pi}\big[(\theta-\pi)\sin\theta + \cos\theta\big], \qquad B_1(\theta) = C_1^{(B)}\cos 2\theta,\\
&B_2(\theta) = -\frac{k^2R^2}{2}\cos\theta C_0^{(B)} + C_3^{(B)}\cos 3\theta + \frac{4R}{3\pi}\Big[\big(k^2R^2/6 - 1/3\big)\cos^3\theta\\
&\qquad - \big(5k^2R^2/4 - 1/4\big)\cos\theta - \frac{1}{2}\sin\theta(\pi-\theta)\big\{2\cos^2\theta\big(k^2R^2-2\big) + 1 - 2k^2R^2\big\}\Big],\\
&B_3(\theta) = \frac{k^2R^2}{3}(2\sin 2\theta - \sin 4\theta)C_0^{(B)} + C_3^{(B)}\cos 4\theta + \frac{4k^2}{R^3}3\pi\Big[\theta\big\{\cos^2 2\theta + 1/4\big\}\\
&\qquad + \Big\{\pi - \theta - \frac{1}{8}\sin 2\theta\Big\}\cos 2\theta + \frac{4}{3}\sin 2\theta - \frac{2}{3}\sin 4\theta - \frac{3}{4}\pi\Big].
\end{aligned} \tag{89}
$$

The asymptotic expansion at $(-R, 0)$ is obtained by an even reflection about the y axis.

Test 5 In this test, the Neumann boundary data undergo a jump discontinuity in the first derivative,

$$
\frac{\partial u}{\partial r}\bigg|_{r=R} = \begin{cases} \pi/2 - \varphi, & 0 < \varphi < \pi,\\ \varphi - 3\pi/2, & \pi < \varphi < 2\pi. \end{cases}
$$

In terms of (ρ, θ), we have (in accordance with the comment right after Eq. (87)):

$$
\begin{aligned}
&\frac{\partial u}{\partial \theta}\bigg|_{\theta=0} = -\frac{2R\rho}{1+\rho^2}\left(\frac{\pi}{2} + \arctan\frac{2\rho}{\rho^2-1}\right) \underset{\rho\to 0}{\approx} -R\left(\pi\rho - 4\rho^2 - \pi\rho^3 + \frac{16}{3}\rho^4 + \ldots\right),\\
&\frac{\partial u}{\partial \theta}\bigg|_{\theta=\pi} = \frac{2R\rho}{1+\rho^2}\left(\frac{\pi}{2} + \arctan\frac{2\rho}{\rho^2-1}\right) \underset{\rho\to 0}{\approx} R\left(\pi\rho - 4\rho^2 - \pi\rho^3 + \frac{16}{3}\rho^4 + \ldots\right).
\end{aligned}
$$

The coefficients of expansion (49) at the point $(R, 0)$ are as follows:

$$
\begin{aligned}
&A_0(\theta) = A_2(\theta) = 0, \qquad A_1(\theta) = \frac{4R}{\pi}\cos 2\theta,\\
&A_3(\theta) = \frac{1}{3\pi}\big[2R\big(k^2R^2-4\big)\cos 4\theta - 4k^2R^3\cos 2\theta\big],
\end{aligned} \tag{90}
$$

$$
\begin{aligned}
&B_0(\theta) = C_0^{(B)}\cos\theta - \pi R\sin\theta, \qquad B_1(\theta) = C_1^{(B)}\cos 2\theta - \frac{2R}{\pi}\big[(2\theta-\pi)\sin 2\theta + \cos 2\theta\big],\\
&B_2(\theta) = -\frac{k^2R^2}{2}\cos\theta C_0^{(B)} + C_2^{(B)}\cos 3\theta - \frac{\pi R}{6}\big[\big(k^2R^2-2\big)\sin 3\theta - 3k^2R^2\sin\theta\big],\\
&B_3(\theta) = -\frac{k^2R^2}{3}(\sin 4\theta - 2\sin 2\theta)C_0^{(B)} - \frac{k^2R^2}{3}\cos 2\theta C_1^{(B)} + \cos 4\theta C_3^{(B)}\\
&\qquad - \frac{4R}{3\pi}\bigg[\left(\frac{1}{8}k^2R^2 - \frac{1}{2}\right)\cos^2 2\theta + \frac{1}{2}\left\{k^2R^2\left(\theta - \frac{\pi}{2}\right) + 2\pi - 4\theta\right\}\sin 4\theta\\
&\qquad - \frac{k^2R^2}{2}\left(\pi^2 + \frac{5}{3}\right)\cos 2\theta - k^2R^2\left(\theta - \frac{\pi}{2}\right)\sin 2\theta + \frac{1}{4} + \frac{3k^2R^2}{8}\left(\pi^2 - \frac{1}{6}\right)\bigg].
\end{aligned} \tag{91}
$$

The asymptotic expansion at $(-R, 0)$ is obtained by an odd reflection about the y axis.

Test 6 This final test employs the boundary data with a discontinuity in the second derivative:

$$
\frac{\partial u}{\partial r}\bigg|_{r=R} = \begin{cases} \cos\varphi, & 0 < \varphi < \pi,\\ \cos 3\varphi, & \pi < \varphi < 2\pi. \end{cases}
$$

In terms of (ρ, θ), the boundary conditions read:

$$
\begin{aligned}
&\frac{\partial u}{\partial \theta}\bigg|_{\theta=0} = -\frac{2R\rho}{1+\rho^2}\cos\left(\arctan\frac{2\rho}{\rho^2-1}\right) \underset{\rho\to 0}{\approx} R\big(-2\rho + 6\rho^3 - 10\rho^5 + \ldots\big),\\
&\frac{\partial u}{\partial \theta}\bigg|_{\theta=\pi} = \frac{2R\rho}{1+\rho^2}\cos\left(3\arctan\frac{2\rho}{\rho^2-1}\right) \underset{\rho\to 0}{\approx} R\big(2\rho - 38\rho^3 + 170\rho^5 - \ldots\big).
\end{aligned}
$$

The coefficients of expansion (49) at the point $(R,0)$ are given by

$$A_0(\theta)=A_1(\theta)=A_3(\theta)=0, \qquad A_2(\theta)=\frac{32R}{3\pi}\cos 3\theta, \tag{92}$$

$$\begin{aligned}
B_0(\theta)&=C_0^{(B)}\cos\theta-2R\sin\theta, \qquad B_1(\theta)=C_1^{(B)}\cos 2\theta,\\
B_2(\theta)&=-\frac{k^2R^2}{2}\cos\theta C_0^{(B)}+C_2^{(B)}\cos 3\theta-\frac{4R}{3\pi}\Big[\big\{\pi\left(k^2R^2-6\right)-32\theta\big\}\cos^2\theta\sin\theta\\
&\quad+\left(\frac{3\pi}{2}-\pi k^2R^2+8\theta\right)\sin\theta-\frac{16}{3}\cos^3\theta+4\cos\theta\Big],\\
B_3(\theta)&=-\frac{k^2R^2}{3}(\sin 4\theta-2\sin 2\theta)C_0^{(B)}-\frac{k^2R^2}{3}\cos 2\theta C_1^{(B)}+\cos 4\theta C_3^{(B)}+\frac{k^2R^3}{3}(4\cos 2\theta-3).
\end{aligned} \tag{93}$$

The asymptotic expansion at $(-R,0)$ is obtained by an odd reflection about the y axis.

References

[1] I.M. Babuška, S.A. Sauter, Is the pollution effect of the FEM avoidable for the Helmholtz equation considering high wave numbers?, SIAM Rev. 42 (3) (2000) 451–484 (electronic), reprint of SIAM J. Numer. Anal. 34 (6) (1997) 2392–2423 [MR1480387 (99b:65135)].

[2] A. Bayliss, C.I. Goldstein, E. Turkel, On accuracy conditions for the numerical computation of waves, J. Comput. Phys. 59 (3) (1985) 396–404.

[3] S. Britt, S. Tsynkov, E. Turkel, Numerical simulation of time-harmonic waves in inhomogeneous media using compact high order schemes, Commun. Comput. Phys. 9 (3) (2011) 520–541, http://dx.doi.org/10.4208/cicp.091209.080410s.

[4] S. Britt, S. Tsynkov, E. Turkel, A high order numerical method for the Helmholtz equation with non-standard boundary conditions, SIAM J. Sci. Comput. 35 (5) (2013) A2255–A2292.

[5] A.P. Calderon, Boundary-value problems for elliptic equations, in: Proceedings of the Soviet–American Conference on Partial Differential Equations in Novosibirsk, Fizmatgiz, Moscow, 1963, pp. 303–304.

[6] A. Deraemaeker, I.M. Babuška, P. Bouillard, Dispersion and pollution of the FEM solution for the Helmholtz equation in one, two and three dimensions, Int. J. Numer. Methods Eng. 46 (1999) 471–499.

[7] L. Fox, R. Sankar, Boundary singularities in linear elliptic differential equations, J. Inst. Math. Appl. 5 (1969) 340–350.

[8] I. Harari, E. Turkel, Accurate finite difference methods for time-harmonic wave propagation, J. Comput. Phys. 119 (2) (1995) 252–270.

[9] F. Ihlenburg, Finite Element Analysis of Acoustic Scattering, Applied Mathematical Sciences, vol. 132, Springer, 1998.

[10] D.S. Kamenetskii, A numerical method for solving a singular boundary value problem for the Chaplygin equation in the hodograph plane, Preprint 60, Keldysh Institute for Applied Mathematics, Russian Academy of Sciences, Moscow, Russia, 1992 [Russian].

[11] D.S. Kamenetskii, V.S. Ryaben'kii, Solution of boundary value problems for the Laplace equation in a domain with a cut by the method of difference potentials, Preprint 33, Keldysh Institute for Applied Mathematics, USSR Academy of Sciences, Moscow, USSR, 1990 [Russian].

[12] D.S. Kamenetskii, E.G. Shifrin, Design of nozzle blades of a gas turbine by the method of hodograph, Preprint 61, Keldysh Institute for Applied Mathematics, Russian Academy of Sciences, Moscow, Russia, 1992 [Russian].

[13] M. Medvinsky, S. Tsynkov, E. Turkel, The method of difference potentials for the Helmholtz equation using compact high order schemes, J. Sci. Comput. 53 (1) (2012) 150–193, http://dx.doi.org/10.1007/s10915-012-9602-y.

[14] M. Medvinsky, S. Tsynkov, E. Turkel, High order numerical simulation of the transmission and scattering of waves using the method of difference potentials, J. Comput. Phys. 243 (2013) 305–322, http://dx.doi.org/10.1016/j.jcp.2013.03.014.

[15] V.S. Ryaben'kii, Method of Difference Potentials and Its Applications, Springer Series in Computational Mathematics, vol. 30, Springer-Verlag, Berlin, 2002.

[16] R.T. Seeley, Singular integrals and boundary value problems, Am. J. Math. 88 (1966) 781–809.

[17] I. Singer, E. Turkel, High-order finite difference methods for the Helmholtz equation, Comput. Methods Appl. Mech. Eng. 163 (1–4) (1998) 343–358.

[18] E. Turkel, D. Gordon, R. Gordon, S. Tsynkov, Compact 2D and 3D sixth order schemes for the Helmholtz equation with variable wave number, J. Comput. Phys. 232 (1) (2013) 272–287, http://dx.doi.org/10.1016/j.jcp.2012.08.016.